Investigation of Neoclassical Tearing Mode Detection by ECE Radiometry in an ITER-like Tokamak via Asymptotic Matching Techniques

Richard Fitzpatrick [a]

Institute for Fusion Studies, Department of Physics,

University of Texas at Austin, Austin TX 78712

The TJ toroidal tearing mode code is used to make realistic predictions of the electron cyclotron emission (ECE) signals generated by neoclassical tearing modes (NTMs) in an ITER-like tokamak plasma equilibrium. In the so-called "outer region", which comprises the bulk of the plasma, helical harmonics of the magnetic field with the same toroidal mode number as the NTM, but different poloidal mode numbers, are coupled together by the Shafranov shifts and shaping of the equilibrium magnetic flux-surfaces. In the "inner region", which is localized in the vicinity of the NTM rational surface, helical harmonics whose poloidal and toroidal mode numbers are in the same ratio as those of the NTM are coupled together nonlinearly to produce a radially asymmetric magnetic island chain. The solutions in the inner and outer regions are asymptotically matched to one another. The asymptotic matching process determines the overall magnetic structure of the NTM, as well as the global perturbation to the electron temperature caused by the mode. A simulated ECE diagnostic is developed that accounts for the downshifting and broadening in frequency of the signal due to the relativistic mass increase of the emitting electrons.

[a] rfitzp@utexas.edu

I. INTRODUCTION

The transient heat fluxes and electromagnetic stresses that the plasma facing components would experience during a disruption in a tokamak fusion reactor are unacceptably large.[1,2] Consequently, such a reactor must be capable of operating reliably in an essentially disruption-free manner. Disruptions in tokamaks are triggered by macroscopic magnetohydrodynamical (MHD) instabilities.[3] Fortunately, disruptions associated with both ideal instabilities and "classical" tearing instabilities can be readily avoided by keeping the toroidal plasma current, the mean plasma pressure, and the mean electron number density below critical values that are either easily calculable or well-known empirically.[1]

A tearing mode[4] of finite amplitude generates a helical magnetic island chain[5] in the vicinity of the rational surface[6] at which it reconnects magnetic flux. If the radial width of the island chain exceeds a relatively small threshold value then rapid heat transport parallel to magnetic field-lines causes a flattening of the electron temperature profile that is localized within the chain's magnetic separatrix.[7] The associated loss of the pressure-gradient-driven non-inductive neoclassical bootstrap current[8] within the separatrix has a destabilizing effect that can render a linearly-stable tearing mode unstable at finite amplitude. This type of instability is known as a "neoclassical tearing mode" (NTM).[9–12] All reactor-relevant tokamak discharges are potentially unstable to 2, 1 and 3, 2 NTMs.[13,14] (Here, m, n denotes a mode whose resonant harmonic has m periods in the poloidal direction, and n periods in the toroidal direction.) It is, therefore, not surprising that NTMs are, by far, the most common cause of disruptions in high-performance tokamak discharges.[1,13–15] Now, an NTM needs to exceed a critical threshold amplitude before it is triggered. In practice, NTMs are triggered by transient magnetic perturbations associated with other more benign instabilities in the plasma, such as sawtooth oscillations, fishbones, and edge localized modes (ELMs).[13,14,16,17] NTMs pose a unique challenge to tokamak fusion reactors because all reactor-relevant tokamak discharges are potentially unstable to multiple NTMs. Moreover, NTM onset is essentially unpredictable, because it is impossible to determine ahead of time which particular sawtooth crash, fishbone, or ELM is going to trigger a particular NTM.[18] Indeed, not all previously documented NTMs possess identifiable triggers.[19]

Neoclassical tearing modes can be suppressed via electron cyclotron current drive (ECCD).[20,21] This technique, which has been successfully implemented on many tokamaks,[22–28] involves launching electron cyclotron waves into the plasma in such a manner that they drive a toroidal current (in the same direction as the equilibrium current) that is localized inside the magnetic separatrix of the NTM island chain. The idea is to compensate for the loss of the bootstrap current inside the separatrix consequent on the local flattening of the electron temperature profile.[13,14]

The successful suppression of an NTM via ECCD depends crucially on the early detection of the mode, combined with an accurate measurement of the instantaneous location of, at least, one of the O-points of the associated island chain.[29] In fact, because the island chain is radially thin, but relatively extended in poloidal and toroidal angle, the measurement of the radial location of the O-point is, by far, the most difficult aspect of this process. The most accurate method of determining the radial location of the O-point is to measure the temperature fluctuations associated with the island chain by means of electron cyclotron emission (ECE) radiometry.[7,30–32]

Given the crucial importance of early and accurate detection of NTMs via ECE radiometry to the success of tokamak fusion reactors, existing theoretical calculations of the expected ECE signal, which are based on single-harmonic cylindrical theory, are surprisingly primitive.[29,32,33] The aim of this paper is to improve such calculations by taking into account the fact that an NTM in a realistic toroidal tokamak equilibrium consists of multiple coupled poloidal and toroidal harmonics. Harmonics with the same toroidal mode number as the NTM, but different poloidal mode numbers, are linearly coupled by the Shafranov shifts, elongations, and triangularities of the equilibrium magnetic flux-surfaces.[34–36] Furthermore, harmonics whose poloidal and toroidal mode numbers are in the same ratio as those of the NTM are coupled nonlinearly in the immediate vicinity of the island chain.[5,7] Previous calculations have taken into account the important fact that an NTM island chain is likely to be radially asymmetric with respect to the rational surface,[37,38] due to the mean radial plasma displacement at the surface, but have not necessarily made an accurate determination of this asymmetry.[29] Our improved calculation incorporates an accurate assessment of the asymmetry. Finally, the ECE signal is downshifted and broadened in frequency due to the relativistic mass increase of the emitting electrons.[30,31,39] This process leads to a shift in the inferred location of the ECE to larger major radius, as well as a radial smearing out the emission. Both of these effects, which limit the accuracy to which the radial location of the island O-point can be measured via ECE, are taken into account in our improved calculation.

The calculation of the magnetic perturbation associated with an NTM is most efficiently formulated as an asymptotic matching problem in which the plasma is divided into two distinct regions.[4,34–36,40–45] In the so-called "outer region", which comprises most of the plasma, the perturbation is governed by the equations of linearized, marginally-stable, ideal-MHD. However, these equations become singular on "rational" magnetic flux-surfaces at which the perturbed magnetic field resonates with the equilibrium field. In the "inner region", which consists of a set of narrow layers centered on the various rational surfaces, non-ideal-MHD effects such as plasma resistivity, as well as nonlinear effects, become important. In the calculation described in this paper, the NTM is assumed to reconnect magnetic flux at one particular rational surface in the plasma (i.e., the $q = 2$ surface for the case of a 2, 1 mode, and the $q = 3/2$ surface in the case of a 3, 2 mode). The response of the plasma at the other rational surfaces is assumed to be ideal, as we would expect to be the case in the presence of sheared plasma rotation.[36] The magnetic perturbation in the segment of the inner region centered on the reconnecting rational surface is that associated with a radially asymmetric magnetic island chain.[5,46] The nonlinear island solution needs to be asymptotically matched to the linear ideal-MHD solution in the outer region. The electron temperature perturbation associated with the NTM in the inner and outer regions is simultaneously determined by the asymptotic matching process.

In this paper, the asymptotic matching is performed using the TJ toroidal tearing mode code,[44,45] which employs an aspect-ratio expanded toroidal magnetic equilibrium.[47] The TJ code is used for the sake of convenience. However, the calculations described in this paper could just as well be implemented in a toroidal tearing mode code, such as STRIDE,[42,43] that employs a general toroidal magnetic equilibrium.

This paper is organized as follows. The adopted plasma equilibrium is described in Sect. II. In Sect. III, the perturbed electron temperature associated with an NTM is calculated in the outer region. The corresponding perturbed electron temperature in the inner region is calculated in Sect. IV. The global perturbed electron temperature, obtained by asymptotically matching the perturbed temperatures in the inner and outer regions, is described in Sect. V. Finally, the paper is summarized, and conclusions are drawn, in Sect. VI.

II. PLASMA EQUILIBRIUM

A. Normalization

Unless otherwise specified, all lengths in this paper are normalized to the major radius of the plasma magnetic axis, R_0, All magnetic field-strengths are normalized to the toroidal field-strength at the magnetic axis, B_0. All plasma pressures are normalized to B_0^2/μ_0.

B. Coordinates

Let R, ϕ, Z be right-handed cylindrical coordinates whose symmetry axis corresponds to the symmetry axis of the axisymmetric toroidal plasma equilibrium. Let r, θ, ϕ be right-handed flux-coordinates whose Jacobian is

$$\mathcal{J}(r,\theta) \equiv (\nabla r \times \nabla\theta \cdot \nabla\phi)^{-1} = r\,R^2. \tag{1}$$

Note that $r = r(R, Z)$ and $\theta = \theta(R, Z)$. The magnetic axis corresponds to $r = 0$, and the plasma-vacuum interface to $r = a$. Here, $a \ll 1$ is the effective inverse aspect-ratio of the plasma.

C. Equilibrium Magnetic Field

Consider a tokamak plasma equilibrium whose magnetic field takes the form

$$\mathbf{B}(r,\theta) = f(r)\,\nabla\phi \times \nabla r + g(r)\,\nabla\phi = f\,\nabla(\phi - q\,\theta) \times \nabla r, \tag{2}$$

where $q(r) = r\,g/f$ is the safety-factor profile. Equilibrium force balance requires that $\nabla P = \mathbf{J} \times \mathbf{B}$, where

$$P(r) = a^2\,p_2(r), \tag{3}$$

is the equilibrium scalar plasma pressure profile, and $\mathbf{J} = \nabla\times\mathbf{B}$ the equilibrium plasma current density. The (unnormalized) equilibrium electron temperature profile is written

$$T_{e\,0}(r) = \frac{B_0^{\,2}}{\mu_0}\,\frac{P(r)}{2\,n_e(r)} + T_{e\,\mathrm{ped}}, \tag{4}$$

where $n_e(r)$ is the (unnormalized) equilibrium electron number density profile. Here, we are assuming that the electrons and ions have the same temperature, as is likely to be the case in a tokamak fusion reactor.

D. Equilibrium Magnetic Flux-Surfaces

The loci of the up-down symmetric equilibrium magnetic flux-surfaces are written in the parametric form [36]

$$R(\hat{r},\omega) = 1 - a\,\hat{r}\,\cos\omega + a^2\left[H_1(\hat{r})\,\cos\omega + H_2(\hat{r})\,\cos 2\,\omega + H_3(\hat{r})\,\cos 3\,\omega\right], \tag{5}$$

$$Z(\hat{r},\omega) = a\,\hat{r}\,\sin\omega + a^2\left[H_2(\hat{r})\,\sin 2\,\omega + H_3(\hat{r})\,\sin 3\,\omega\right], \tag{6}$$

where $r = a\,\hat{r}$. Here, the dimensionless functions $H_1(\hat{r})$, $H_2(\hat{r})$, and $H_3(\hat{r})$ control the Shafranov shifts, vertical elongations, and triangularities of the flux-surfaces, respectively. Moreover,[47]

$$g(\hat{r}) = 1 + a^2\,g_2(\hat{r}), \tag{7}$$

$$g_2' = -p_2' - \frac{\hat{r}}{q^2}\,(2-s), \tag{8}$$

$$H_1'' = -(3-2\,s)\,\frac{H_1'}{\hat{r}} - 1 + \frac{2\,p_2'\,q^2}{\hat{r}}, \tag{9}$$

$$H_j'' = -(3-2\,s)\,\frac{H_j'}{\hat{r}} + (j^2-1)\,\frac{H_j}{\hat{r}^{\,2}} \qquad \text{for } j>1, \tag{10}$$

$$\theta = \omega + a\,\hat{r}\,\sin\omega - a\sum_{j=1,3}\frac{1}{j}\left[H_j' - (j-1)\,\frac{H_j}{\hat{r}}\right]\sin j\,\omega, \tag{11}$$

where $s(\hat{r}) = \hat{r}\,q'/q$ is the magnetic shear, and $'$ denotes $d/d\hat{r}$. The plasma equilibrium is fully specified by the value of a, the two free flux-surface functions $q(\hat{r})$ and $p_2(\hat{r})$, and the values of $H_2(1)$ and $H_3(1)$.

E. Example Plasma Equilibrium

Figures 1 and 2 show the magnetic flux-surfaces and profiles of an ITER-like example plasma equilibrium characterized by $B_0 = 5.3$ T, $R_0 = 6.2$ m, $a = 0.2$, $H_2(1) = 1.0$, and $H_3(1) = 0.5$. The toroidal plasma current is $I_t = 2.5\,\mathrm{MA}$. (This rather low value is symptomatic of the fact that the true ITER inverse aspect-ratio is 0.32 rather than 0.20.) The normalized plasma inductance is $l_i = 1.16$. Finally, the normalized beta is $\beta_N = 1.32$.

III. PERTURBED ELECTRON TEMPERATURE IN OUTER REGION

A. Perturbation in Outer Region

Let the positive integer n be the toroidal mode number of the NTM. Let there be K rational surfaces in the plasma, of minor radius r_k (for $k = 1, K$), at which the resonance condition $q(r_k) = m_k/n$ is satisfied, where the positive integer m_k is the resonant poloidal mode number at the kth surface. The perturbed magnetic field in the outer region is specified by [44,45]

$$b^r(r,\theta,\phi) \equiv \mathbf{b}\cdot\nabla r = \frac{\mathrm{i}}{r\,R^2}\sum_{j=1,J}\psi_{m_j}(r)\,\mathrm{e}^{\,\mathrm{i}\,(m_j\,\theta-n\,\phi)}. \tag{12}$$

Here, $\mathbf{b}(r,\theta,\phi)$ is the perturbed magnetic field-strength, and the m_j are the $J > K$ poloidal mode numbers included in the calculation. (The m_k are a subset of the m_j.)

The functions $\psi_{m_j}(r)$ are determined by solving a set of $2\,J$ coupled ordinary differential equations that are singular at the various rational surfaces in the plasma. The solutions to these equations must be launched from the magnetic axis ($r = 0$), integrated outward in r, stopped just before and restarted just after each rational surface in the plasma, integrated to the plasma boundary ($r = a$), and then matched to a free-boundary vacuum solution. This process is described in detail in Ref. 44.

B. Behavior in Vicinity of Rational Surface

Consider the behavior of the $\psi_{m_j}(r)$ in the vicinity of the kth rational surface. The non-resonant $\psi_{m_j}(r)$, for which $m_j \neq m_k$, are continuous across the surface. On the other hand, the resonant $\psi_{m_j}(r)$ is such that

$$\psi_{m_k}(r_k + x) = A_{L\,k}\,|x|^{\nu_{L\,k}} + \mathrm{sgn}(x)\,A^{\pm}_{S\,k}\,|x|^{\nu_{S\,k}}, \tag{13}$$

$$\tag{14}$$

where

$$\nu_{L\,k} = \frac{1}{2} - \sqrt{-D_{I\,k}}, \tag{15}$$

$$\nu_{S\,k} = \frac{1}{2} + \sqrt{-D_{I\,k}}, \tag{16}$$

$$D_{I\,k} = -\left[\frac{2\,(1-q^2)}{s^2}\,r\,\frac{dP}{dr}\right]_{r_k} - \frac{1}{4} \tag{17}$$

Here, $A_{L\,k}$ is termed the coefficient of the "large" solution, whereas $A^{\pm}_{S\,k}$ are the coefficients of the "small" solution. Here, $A^{+}_{S\,k}$ corresponds to the region $x > 0$, whereas $A^{-}_{S\,k}$ corresponds to the region $x < 0$. Furthermore, $D_{I\,k}$ is the ideal Mercier interchange parameter (which needs to be negative to ensure stability to localized interchange modes),[48–50] and $\nu_{L\,k}$ and $\nu_{S\,k}$ are termed the Mercier indices.

It is helpful to define the quantities[44]

$$\Psi_k = r_k^{\,\nu_{L\,k}}\left(\frac{\nu_{S\,k}-\nu_{L\,k}}{L^{m_k}_{m_k}}\right)^{1/2}_{r_k} A_{L\,k}, \tag{18}$$

$$\Delta\Psi_k = r_k^{\,\nu_{S\,k}}\left(\frac{\nu_{S\,k}-\nu_{L\,k}}{L^{m_k}_{m_k}}\right)^{1/2}_{r_k} (A^{+}_{S\,k} - A^{-}_{S\,k}), \tag{19}$$

at each rational surface in the plasma, where

$$L^{m_k}_{m_k}(r) = m_k^2\,c^{m_k}_{m_k}(r) + n^2\,r^2, \tag{20}$$

$$c^{m_k}_{m_k}(r) = \oint |\nabla r|^{-2}\,\frac{d\theta}{2\pi}. \tag{21}$$

Here, the dimensionless complex parameter Ψ_k is a measure of the reconnected helical magnetic flux at the kth rational surface, whereas the dimensionless complex parameter $\Delta\Psi_k$ is a measure of the strength of a localized current sheet that flows parallel to the equilibrium magnetic field at the surface.

It is assumed that $\Psi_k = 0$ for all k, except for $k = l$. In other words, the NTM only reconnects magnetic flux at the lth rational surface. Let

$$\psi_{m_j}(r) = \Psi\,\hat{\psi}_{m_j}(r), \tag{22}$$

where Ψ is the reconnected magnetic flux at the lth rational surface, and the $\hat{\psi}_{m_j}(r)$ are normalized such that $\Psi_k = \delta_{kl}$.

C. Electron Temperature in Outer Region

Let $\boldsymbol{\xi}(r,\theta,\phi)$ be the plasma displacement in the outer region. We can write [45]

$$\begin{aligned}\xi^r(r,\theta,\phi) \equiv \boldsymbol{\xi}\cdot\nabla r &= \sum_{j=1,J} \xi^r_{m_j}(r)\,\mathrm{e}^{\,\mathrm{i}\,(m_j\,\theta - n\,\phi)}\\ &= \Psi\,\frac{q}{r\,g}\sum_{j=1,J}\frac{\hat{\psi}_{m_j}}{m_j - n\,q}\,\mathrm{e}^{\,\mathrm{i}\,(m_j\,\theta-n\,\phi)}.\end{aligned} \tag{23}$$

The perturbed electron temperature in the outer region is written

$$\delta T_e(r,\theta,\phi) = -\frac{dT_{e\,0}}{dr}\,\xi^r(r,\theta,\phi) + \delta T_{e\,0}\,H(r-r_l) \tag{24}$$

where

$$H(x) = \begin{cases} 1 & x < 0\\ 0 & x > 0\end{cases}. \tag{25}$$

Here, we are assuming that the electron temperature is passively convected by the plasma in the outer region. We are also assuming that there is no change in topology of the magnetic flux-surfaces in the outer region. In other words, any topology changes are confined to the inner region. Finally, $\delta T_{e\,0} < 0$ is the reduction in the equilibrium electron temperature in the plasma core due to the flattening of the temperature profile in the vicinity of the NTM island chain.[51]

IV. PERTURBED ELECTRON TEMPERATURE IN INNER REGION

A. Introduction

Consider the segment of the inner region in the vicinity of the lth rational surface, where the NTM reconnects magnetic flux. Let $x = r - r_l$, $X = x/W$, and $\zeta = m_l\,\theta - n\,\phi$, where $W \ll a$ is the full width of the NTM island chain's magnetic separatrix. Here, m_l is the resonant poloidal mode number at the lth rational surface. Let us search for a single-helicity solution in which the magnetic flux-surfaces in the vicinity of the island chain are contours of some function $\Omega(X,\zeta)$. Now, a magnetic island chain whose width exceeds the linear layer width is a helical magnetic equilibrium.[5] As such, the island magnetic-flux surfaces must satisfy the fundamental force balance requirement [46]

$$\left[\left.\frac{\partial^2\Omega}{\partial X^2}\right|_\zeta, \Omega\right] = 0, \tag{26}$$

where

$$[A,B] \equiv \left.\frac{\partial A}{\partial X}\right|_\zeta \left.\frac{\partial B}{\partial \zeta}\right|_X - \left.\frac{\partial B}{\partial X}\right|_\zeta \left.\frac{\partial A}{\partial \zeta}\right|_X. \tag{27}$$

This requirement stipulates that the current density in the island region must be constant on magnetic flux-surfaces.

B. Island Magnetic Flux-Surfaces

A suitable solution of Eq. (26) that connects to the ideal-MHD solution in the outer region is [46]

$$\Omega(X,\zeta) = 8\,X^2 + \cos(\zeta - \delta^2\,\sin\zeta) - 2\sqrt{8}\,\delta\,X\,\cos\zeta + \delta^2\,\cos^2\zeta, \tag{28}$$

where $|\delta| < 1$. As illustrated in Fig. 3, the magnetic flux-surfaces (i.e., the contours of Ω) map out an asymmetric (with respect to $X = 0$) island chain whose X-points lie at $X = \delta/\sqrt{8}$, $\zeta = 0,\ 2\pi$, and $\Omega = +1$, and whose O-points lie at $X = -\delta/\sqrt{8}$, $\zeta = \pi$, and $\Omega = -1$. The maximum width of the magnetic separatrix (in x) is W.

The first term on the right-hand side of Eq. (28) emanates from the unperturbed (by the NTM) plasma equilibrium, whereas the remaining terms emanate from the NTM perturbation in the outer region. In particular, the third term on the right-hand side, which governs the island asymmetry, originates from the mean radial gradient in the $\cos\zeta$ component of the linear NTM eigenfunction at the rational surface.

The island asymmetry is characterized by the dimensionless parameter δ. If $\delta > 0$ then the island O-points are displaced radially inward (with respect to the unperturbed rational surface), whereas the X-points are displaced radially outward an equal distance. The opposite is the case if $\delta < 0$. Generally speaking, we expect $\delta > 0$ for NTMs (because the linear eigenfunctions for such modes tend to attain their maximum amplitudes inside the rational surface; see Fig. 2 in Ref. 52). Note that if $|\delta|$ exceeds the critical value unity then the X-points bifurcate, and a current sheet forms between them.[53] Consequently, it is no longer possible to analyze the resistive evolution of the resulting island chain using a variant of standard Rutherford island theory.[5] Hence, we shall only consider the case $-1 \leq \delta < 1$.

C. Coordinate Transformation

Let us define the new coordinates[46]

$$Y = X - \frac{\delta}{\sqrt{8}}\cos\zeta, \tag{29}$$

$$\xi = \zeta - \delta^2 \sin\zeta. \tag{30}$$

When expressed in terms of these coordinates, the magnetic flux-function (28) reduces to the simple form

$$\Omega(Y,\xi) = 8\,Y^2 + \cos\xi. \tag{31}$$

Thus, as illustrated in Fig. 4, irrespective of the value of the asymmetry parameter, δ, when plotted in Y, ξ space, the magnetic flux-surfaces map out a symmetric (with respect to $Y = 0$) island chain whose O-points lie at $\xi = \pi$, $Y = 0$, and $\Omega = -1$, and whose X-points lie at $\xi = 0$, 2π, $Y = 0$, and $\Omega = +1$. The fact that the radially asymmetric island flux-surfaces can be remapped to a set of radially symmetric surfaces greatly simplifies our calculation.

The inversion of Eq. (30) is very well known: [54]

$$\zeta = \xi + 2\sum_{\mu=1,\infty}\left[\frac{J_\mu(\mu\,\delta^2)}{\mu}\right]\sin(\mu\,\xi), \tag{32}$$

$$\cos\zeta = -\frac{\delta^2}{2} + \sum_{\mu=1,\infty}\left[\frac{J_{\mu-1}(\mu\,\delta^2)-J_{\mu+1}(\mu\,\delta^2)}{\mu}\right]\cos(\mu\,\xi), \tag{33}$$

$$\sin\zeta = \frac{2}{\delta^2}\sum_{\mu=1,\infty}\left[\frac{J_\mu(\mu\,\delta^2)}{\mu}\right]\sin(\mu\,\xi), \tag{34}$$

$$\cos(\nu\,\zeta) = \nu\sum_{\mu=1,\infty}\left[\frac{J_{\mu-\nu}(\mu\,\delta^2)-J_{\mu+\nu}(\mu\,\delta^2)}{\mu}\right]\cos(\mu\,\xi), \tag{35}$$

$$\sin(\nu\,\zeta) = \nu\sum_{\mu=1,\infty}\left[\frac{J_{\mu-\nu}(\mu\,\delta^2)+J_{\mu+\nu}(\mu\,\delta^2)}{\mu}\right]\cos(\mu\,\xi), \tag{36}$$

for $\nu > 1$.

D. Plasma Displacement

Outside the magnetic separatrix, we can write

$$\Omega(X,\zeta) = 8\,(X-\Xi)^2, \tag{37}$$

where $\Xi = \xi^r/W$ is the normalized radial plasma displacement. It follows that, in the limit $|X| \gg 1$,

$$\begin{aligned}\Xi(X,\zeta) &= -\frac{[\Omega(X,\zeta)-8\,X^2-8\,\Xi^2]}{16\,X}\\ &= \frac{\delta}{\sqrt{8}}\cos\zeta - \frac{\cos(\zeta-\delta^2\,\sin\zeta)+\delta^2\,\cos^2\zeta}{16\,X}+\frac{\Xi^2}{2\,X}\\ &\simeq \frac{\delta}{\sqrt{8}}\cos\zeta - \frac{\cos(\zeta-\delta^2\,\sin\zeta)}{16\,X},\end{aligned} \tag{38}$$

where use has been made of Eq. (28). Note that $\Xi(X,\zeta)$ is an even function of ζ. Let us write

$$\Xi(X,\zeta) = \sum_{\nu=0,\infty}\Xi_\nu(X)\,\cos(\nu\,\zeta). \tag{39}$$

Thus,

$$\Xi_1(X) = 2\oint\Xi(X,\zeta)\,\cos(\zeta)\,\frac{d\zeta}{2\pi} = \frac{\delta}{\sqrt{8}} - \frac{1}{8\,X}\oint\cos(\zeta-\delta^2\,\sin\zeta)\,\cos\zeta\,\frac{d\zeta}{2\pi}$$

$$= \frac{\delta}{\sqrt{8}} - \frac{1}{16\,X}\oint \cos(-\delta^2\,\sin\zeta)\,\cos\zeta\,\frac{d\zeta}{2\pi}$$
$$- \frac{1}{16\,X}\oint \cos(2\,\zeta-\delta^2\,\sin\zeta)\,\cos\zeta\,\frac{d\zeta}{2\pi}. \tag{40}$$

But,[54,55]

$$J_\nu(\delta^2) = \oint \cos(\nu\,\zeta - \delta^2\,\sin\zeta)\,\frac{d\zeta}{2\pi}, \tag{41}$$

so

$$\Xi_1(X) = \frac{\delta}{\sqrt{8}} - \frac{J_0(\delta^2)+J_2(\delta^2)}{16\,X}, \tag{42}$$

and

$$\xi_1^r(r_l+x) = \frac{W\,\delta}{\sqrt{8}} - \frac{W^2}{16\,x}\,[J_0(\delta^2)+J_2(\delta^2)]. \tag{43}$$

In the outer region, $\xi^r_{m_l}(r)$ is the equivalent quantity to $\xi^r_1(r)$. It follows from Eq. (23) that, in the limit $|x|\ll a$,

$$\xi^r_{m_l}(r_l+x) = \Psi\,\frac{q}{r\,g}\,\frac{\hat{\psi}_{m_l}}{m_l-n\,q} = -\Psi\left(\frac{h\,q}{s\,q}\right)_{r_l}\frac{1}{x}+\mathcal{O}(1), \tag{44}$$

where

$$h(r) = \frac{(L^{m_l}_{m_l})^{1/2}}{m_l}, \tag{45}$$

and use has been made of Eqs. (13) and (18). Here, we are assuming that $\nu_{L\,l}\simeq 0$ and $\nu_{S\,l}\simeq 1$, as is generally the case in a large aspect-ratio tokamak. A comparison between Eqs. (43) and (44) reveals that

$$\Psi = \left(\frac{W}{4}\right)^2\left(\frac{s\,g}{h\,q}\right)_{r_l}\left[J_0(\delta^2)+J_2(\delta^2)\right], \tag{46}$$

and

$$\delta \simeq \frac{\sqrt{2}}{W}\left[\xi^r_{m_l}(r_l+W)+\xi^r_{m_l}(r_l-W)\right]. \tag{47}$$

Equation (46) gives the relationship between the reconnected magnetic flux, Ψ, and the island width, W. This relationship differs from the conventional one[5] because of corrections due to the radial asymmetry of the island chain. However, the corrections are fairly minor. In fact, $1\geq J_0(\delta^2)+J_2(\delta^2)\geq 0.880$ for $0\leq|\delta|\leq 1$. Equation (47) specifies the relationship between the island asymmetry parameter, δ, and the mean radial plasma displacement at the rational surface. Note that the matching between the inner and outer solutions is performed at $r=r_l\pm W$.

E. Flux-Surface Average Operator

Now,

$$\left.\frac{\partial}{\partial X}\right|_{\zeta} = \left.\frac{\partial \Omega}{\partial X}\right|_{\zeta}\left.\frac{\partial}{\partial \Omega}\right|_{\xi} + \left.\frac{\partial \xi}{\partial X}\right|_{\zeta}\left.\frac{\partial}{\partial \xi}\right|_{\Omega} = 16\,Y\left.\frac{\partial}{\partial \Omega}\right|_{\xi}, \tag{48}$$

and

$$\left.\frac{\partial}{\partial \zeta}\right|_{X} = \left.\frac{\partial \Omega}{\partial \zeta}\right|_{X}\left.\frac{\partial}{\partial \Omega}\right|_{\xi} + \left.\frac{\partial \xi}{\partial \zeta}\right|_{X}\left.\frac{\partial}{\partial \xi}\right|_{\Omega}, \tag{49}$$

so

$$[A,B] \equiv \frac{16\,Y}{\sigma}\left(\left.\frac{\partial A}{\partial \Omega}\right|_{\xi}\left.\frac{\partial B}{\partial \xi}\right|_{\Omega} - \left.\frac{\partial B}{\partial \Omega}\right|_{\xi}\left.\frac{\partial A}{\partial \xi}\right|_{\Omega}\right), \tag{50}$$

where

$$\sigma(\xi) \equiv \frac{d\zeta}{d\xi} = 1 + 2\sum_{\mu=1,\infty} J_\mu(\mu\,\delta^2)\,\cos(\mu\,\xi), \tag{51}$$

and use has been made of Eqs. (27)–(30) and (32). In particular,

$$[A,\Omega] = -\frac{16\,Y}{\sigma}\left.\frac{\partial A}{\partial \xi}\right|_{\Omega}. \tag{52}$$

The flux-surface average operator, $\langle\cdots\rangle$, is the annihilator of $[A,\Omega]$ for arbitrary $A(\varsigma,\Omega,\xi)$.[7,46] Here, $\varsigma = +1$ for $Y>0$ and $\varsigma=-1$ for $Y<0$. It follows from Eq. (52) that

$$\langle A\rangle = \int_{\zeta_0}^{2\pi-\zeta_0} \frac{\sigma(\xi)\,A_+(\Omega,\xi)}{\sqrt{2\,(\Omega-\cos\xi)}}\,\frac{d\xi}{2\pi} \tag{53}$$

for $-1\leq\Omega\leq 1$, and

$$\langle A\rangle = \int_{0}^{2\pi} \frac{\sigma(\xi)\,A(\varsigma,\Omega,\xi)}{\sqrt{2\,(\Omega-\cos\xi)}}\,\frac{d\xi}{2\pi} \tag{54}$$

for $\Omega>1$. Here, $\xi_0 = \cos^{-1}(\Omega)$, and

$$A_+(\Omega,\xi) = \frac{1}{2}\left[A(+1,\Omega,\xi) + A(-1,\Omega,\xi)\right]. \tag{55}$$

F. Wide Island Limit

In the so-called “wide island limit”, in which parallel electron heat transport dominates perpendicular heat transport,[7,46] the electron temperature in the vicinity of the island chain can be written

$$T_e(X,\zeta) = T_{e\,l} + \varsigma\,W\,T_{e\,l}'\,\tilde{T}(\Omega), \tag{56}$$

where $T_{el} = T_{e0}(r_l)$ and $T'_{el} = dT_{e0}(r_l)/dr$ are the equilibrium electron temperature and temperature gradient, respectively, at the island rational surface. Here, $\tilde{T}(\Omega)$ satisfies[7]

$$\left\langle \left. \frac{\partial^2 \tilde{T}}{\partial X^2} \right|_{\zeta} \right\rangle = 0, \tag{57}$$

subject to the boundary condition that

$$\tilde{T}(\Omega) \rightarrow |X| \tag{58}$$

as $|X| \rightarrow \infty$. It follows from Eqs. (31), (48), and (54) that

$$\frac{d}{d\Omega}\left(\langle Y^2 \rangle \frac{d\tilde{T}}{d\Omega}\right) = 0 \tag{59}$$

subject to the boundary condition that

$$\tilde{T}(\Omega) \rightarrow \frac{\Omega^{1/2}}{\sqrt{8}} \tag{60}$$

as $\Omega \rightarrow \infty$. Note that $\tilde{T}(\Omega) = 0$ inside the magnetic separatrix, by symmetry, which implies that the electron temperature profile is completely flattened in the region enclosed by the separatrix.[7]

Outside the separatrix,

$$\langle Y^2 \rangle(\Omega) = \frac{1}{16} \int_0^{2\pi} \sigma(\xi) \sqrt{2\,(\Omega - \cos\xi)}\, \frac{d\xi}{2\pi}. \tag{61}$$

Let

$$\kappa = \left(\frac{1+\Omega}{2}\right)^{1/2}. \tag{62}$$

Thus, the island O-points correspond to $\kappa = 0$, and the magnetic separatrix to $\kappa = 1$. It follows that

$$\langle Y^2 \rangle(\kappa) = \frac{\kappa}{4\pi} \int_0^{\pi/2} \sigma(2\,\vartheta - \pi) \left(1 - \frac{\sin^2\vartheta}{\kappa^2}\right)^{1/2} d\vartheta \tag{63}$$

for $\kappa > 1$. Thus, making use of Eq. (51),

$$\langle Y^2 \rangle(\kappa) = \frac{\kappa}{4\pi}\, G(1/\kappa), \tag{64}$$

where

$$G(p) = E_0(p) + 2\sum_{\mu=1,\infty}\cos(\mu\,\pi)\,J_\mu(\mu\,\delta^2)\,E_\mu(p), \tag{65}$$

$$E_\mu(p) = \int_0^{\pi/2}\cos(2\,\mu\,\vartheta)\,(1-p^2\,\sin^2\vartheta)^{1/2}\,d\vartheta. \tag{66}$$

Equation (59) yields

$$\tilde{T}(\kappa) = 0 \tag{67}$$

for $0\leq\kappa\leq 1$, and

$$\frac{d}{d\kappa}\left[G(1/\kappa)\,\frac{d\tilde{T}}{d\kappa}\right] = 0 \tag{68}$$

for $\kappa > 1$. Thus,

$$\frac{d\tilde{T}}{d\kappa} = \frac{c}{G(1/\kappa)} \tag{69}$$

for $\kappa > 1$, subject to the boundary condition that

$$\tilde{T}(\kappa)\rightarrow\frac{\kappa}{2} \tag{70}$$

as $\kappa\rightarrow\infty$. Now, $E_0(0)=\pi/2$, and $E_{\mu>0}(0)=0$, which implies that $c=\pi/4$. So

$$\frac{d\tilde{T}}{d\kappa} = \frac{\pi}{4}\,\frac{1}{G(1/\kappa)}, \tag{71}$$

$$\tilde{T}(\kappa) = F(\kappa), \tag{72}$$

$$F(\kappa) = \frac{\pi}{4}\int_1^\kappa\frac{d\kappa'}{G(1/\kappa')} \tag{73}$$

for $\kappa > 1$.

G. Helical Harmonics of Perturbed Electron Temperature

We can write

$$\tilde{T}(X,\zeta) = \sum_{\nu=0,\infty}\delta T_\nu(X)\,\cos(\nu\,\zeta). \tag{74}$$

Now,

$$\delta T_0(X) = \oint\tilde{T}(X,\zeta)\,\frac{d\zeta}{2\pi}, \tag{75}$$

where the integral is performed at constant X. It follows from Eqs. (31), (51), (62), and (72) that

$$\delta T_0(X) = \int_0^{\xi_c} F(\kappa)\,\sigma(\xi)\,\frac{d\xi}{\pi}, \tag{76}$$

where

$$\xi_c = \cos^{-1}(1-8\,Y^2) \tag{77}$$

for $|Y|<1/2$, and $\xi_c=\pi$ for $|Y|\geq 1/2$. Furthermore,

$$\kappa = \left[4\,Y^2+\cos^2\left(\frac{\xi}{2}\right)\right]^{1/2}. \tag{78}$$

Let

$$\delta T_{0\,+} = \lim_{X\rightarrow\infty}\left[X-\delta T_0(X)\right], \tag{79}$$

$$\delta T_{0\,-} = -\lim_{X\rightarrow -\infty}\left[X-\delta T_0(X)\right], \tag{80}$$

$$\delta T_{0\,\infty} = \delta T_{0\,+}+\delta T_{0\,-}. \tag{81}$$

The quantity $\delta T_{0\,\infty}$ is related to the reduction of the electron temperature in the plasma core, $\delta T_{e\,0}$, due to the flattening of the temperature profile inside the island separatrix, as follows:

$$\delta T_{e\,0} = W\,T_{e\,l}'\,\delta T_{0\,\infty}. \tag{82}$$

Here, we are assuming that the equilibrium electron temperature at the plasma boundary is fixed.[51] Figure 5 shows $T_{0\,\infty}$ plotted as a function of the modulus of the island asymmetry parameter, $|\delta|$. Note that $T_{0\,\infty}$ is positive, indicating that a magnetic island chain decreases the core electron temperature, assuming that the unperturbed electron temperature gradient at the island rational surface is negative. [See Eq. (82).] It is clear that a symmetric (i.e., $\delta=0$) magnetic island chain give rise to slightly larger reduction in the core temperature than an asymmetric island chain of the same width.

For $\nu>0$, we have

$$\delta T_\nu(X) = 2\oint \tilde{T}(X,\zeta)\,\cos(\nu\,\zeta)\,\frac{d\zeta}{2\pi}, \tag{83}$$

where the integral is performed at constant X. Integrating by parts, we obtain

$$\delta T_\nu(X) = -\frac{2}{\nu}\oint \left.\frac{\partial \tilde{T}}{\partial\zeta}\right|_X \sin(\nu\,\zeta)\,\frac{d\zeta}{2\pi}. \tag{84}$$

But,

$$\left.\frac{\partial \tilde{T}}{\partial\zeta}\right|_X = \frac{d\tilde{T}}{d\kappa}\left.\frac{\partial\kappa}{\partial\zeta}\right|_X = \frac{1}{4\,\kappa}\frac{d\tilde{T}}{d\kappa}\left.\frac{\partial\Omega}{\partial\zeta}\right|_X = -\frac{1}{4\,\kappa}\frac{d\tilde{T}}{d\kappa}\,\tau(\xi), \tag{85}$$

where

$$\tau(\xi) = \sin\xi\,(1-\delta^2\,\cos\zeta) - 2\sqrt{8}\,\delta\,X\,\sin\zeta + \delta^2\,\sin(2\,\zeta), \tag{86}$$

and use has been made of Eqs. (28) and (62). Hence,

$$\delta T_\nu(X) = \frac{1}{8\,\nu}\int_0^{\xi_c}\frac{\sin(\nu\,\zeta)\,\tau(\xi)\,\sigma(\xi)}{\kappa\,G(1/\kappa)}\,d\xi, \tag{87}$$

where use has been made of Eqs. (51) and (71).

Figure 6 shows the harmonics of the normalized electron temperature in the inner region, $\delta T_\nu(x/W)$, calculated for an asymmetric magnetic island characterized by $\delta = 0.5$. Note that the harmonics are asymmetric in X. (By contrast, Fig. 3 of Ref. 7 shows the purely anti-symmetric harmonics of a symmetric island.) It can be seen that the $\nu = 0$ and $\nu = 1$ harmonics extend into the outer region, whereas the $\nu > 1$ harmonics are strongly localized in the vicinity of the island.

Finally, Fig. 7 shows the normalized electron temperature distribution, $\tilde{T}(x/W,\zeta)$, in the vicinity of an asymmetric magnetic island characterized by $\delta = 0.5$. This temperature distribution is reconstructed from 16 helical harmonics (i.e., ν in the range 0 to 15). As expected, the temperature profile is almost completely flattened in the region enclosed within the magnetic separatrix.

H. Modified Rutherford Equation

The nonlinear growth of the magnetic island chain associated with an NTM that is resonant at the lth rational surface is governed by a modified Rutherford equation that takes the form [5,13,46,56,57]

$$G_{\rm ruth}\,\tau_R\,\frac{d}{dt}\left(\frac{W}{r_l}\right) = E_{ll} + \left[\hat{\beta}\,(\alpha_b-\alpha_c)\,G_{\rm boot} + J_{\rm max}\,G_{\rm eccd}\right]\frac{r_l}{W}, \tag{88}$$

where

$$G_{\rm ruth} = 2\int_{-1}^{\infty}\frac{(\langle\cos\xi\rangle+\delta^2\,\langle\sin\xi\,\sin\zeta\rangle)\,\langle\cos\zeta\rangle}{\langle 1\rangle}\,d\Omega, \tag{89}$$

$$G_{\rm boot} = \int_{1}^{\infty}\frac{\langle\cos\zeta\rangle}{\langle 1\rangle\,\langle Y^2\rangle}\,d\Omega, \tag{90}$$

$$G_{\rm eccd} = -16\int_{-1}^{\infty}\frac{\langle J_+\rangle\,\langle\cos\zeta\rangle}{\langle 1\rangle}\,d\Omega, \tag{91}$$

Here, $J_+(x,\zeta)$ is the component of the normalized (such that the peak value is unity) current density profile driven by electron cyclotron waves that is even in Y. Moreover,

$$\tau_R = \left(\frac{\mu_0\,r^2}{\eta_\parallel}\right)_{r_l}, \tag{92}$$

$$\hat{\beta} = \left(\frac{\mu_0\,n_e\,T_{e\,0}}{B_0^{\,2}}\right)_{r_l}\frac{L_s}{L_T} \tag{93}$$

$$L_s = \left(\frac{q}{s}\right)_{r_l}, \tag{94}$$

$$L_T = -\left(\frac{T_{e\,0}}{dT_{e\,0}/dr}\right)_{r_l}, \tag{95}$$

$$\alpha_b = (\beta_{11}-\beta_{12})\,\left(f_t\,\frac{q}{r}\right)_{r_l}, \tag{96}$$

$$f_t = 1.46\,r^{1/2}, \tag{97}$$

$$\alpha_c = \frac{2\,L_s}{L_c}, \tag{98}$$

$$L_c = \left[\frac{1}{r\,(1-1/q^2)-a\,s\,H_1'}\right]_{r_l}. \tag{99}$$

Here, E_{ll} is the normalized linear tearing stability index of an m_l, n tearing mode that only reconnects magnetic flux at the lth rational surface,[36] τ_R is the resistive diffusion timescale, $\eta_\parallel(r)$ the plasma parallel electrical resistivity, $\hat{\beta}$ the normalized electron pressure, L_s the magnetic shear-length, L_T the electron temperature gradient scale-length, L_c the average magnetic field-line curvature scale-length, and f_t the fraction of trapped particles. Moreover, for a plasma with an effective charge number of unity, $\beta_{11}=1.641$ and $\beta_{12}=1.225$.[57] Finally,

$$J_{\rm max} = \frac{\mu_0\,R_0\,L_s}{B_0}\,j_{\rm max}, \tag{100}$$

where $j_{\max}$ is the unnormalized peak current density driven by electron cyclotron waves.

The term in the modified Rutherford equation, (88), that involves α_b represents the destabilizing effect of the loss of the bootstrap current inside the island separatrix consequent on the flattening of the electron temperature profile.[7,59] The term involving α_c represents the stabilizing effect of magnetic field-line curvature consequent on the flattening of the electron temperature profile.[57,60] Finally, the term involving $J_{\max}$ represents the effect of current driven in the island region by electron cyclotron waves.[46] In writing the modified Rutherford equation, we have adopted various large aspect-ratio approximations,[50,57] have assumed that the driven current rapidly equilibrates on island magnetic flux-surfaces, and have neglected the contributions to the equation due to incomplete temperature flattening[7] and the ion polarization current[58] (which are only important for very narrow islands). We have also neglected the contribution due to plasma heating via electron cyclotron waves (which is similar to, but generally smaller than, that of electron cyclotron current drive).[13,46]

The following results are useful when performing flux-surface averages:[46]

$$\langle A(\kappa,\xi)\rangle(\kappa) = \frac{1}{\pi}\int_0^{\pi/2}\frac{\sigma(\xi)\,A(\kappa,\xi)}{\sqrt{1-\kappa^2\,\sin^2\vartheta}}\,d\vartheta \tag{101}$$

for $0\leq\kappa\leq 1$, where $\xi = 2\,\cos^{-1}(\kappa\,\sin\vartheta)$. Likewise,

$$\langle A(\kappa,\xi)\rangle(\kappa) = \frac{1}{\pi}\int_0^{\pi/2}\frac{\sigma(\xi)\,A(\kappa,\xi)}{\sqrt{\kappa^2-\sin^2\vartheta}}\,d\vartheta \tag{102}$$

for $\kappa > 1$, where $\xi = \pi - 2\,\vartheta$. Recall that $\kappa = [(1+\Omega)/2]^{1/2}$.

Table I lists various quantities calculated by the TJ code at the 3, 2 and the 2, 1 rational surfaces for the example plasma equilibrium shown in Figs. 1 and 2. Note that the critical linear tearing stability index that must be exceeded before the stabilizing effect of average magnetic field-line curvature is overcome[45] exceeds the linear tearing stability index for both surfaces. In other words, the 3, 2 and the 2, 1 classical tearing modes are both linearly stable. On the other hand, the difference between the bootstrap parameter, α_b, and the curvature parameter, α_c, is positive for both surfaces. In other words, the 3, 2 and the 2, 1 neoclassical tearing modes are both potentially unstable.

Figure 8 shows the integrals $G_{\rm ruth}$ and $G_{\rm boot}$ evaluated as functions of the modulus of the island asymmetry parameter, $|\delta|$. It can be seen that both integrals only depend weakly on $|\delta|$, as long as $|\delta|$ does not get too close to unity.[38,46] Note that $G_{\rm ruth} = 0.8360$ and $G_{\rm boot} = 6.381$ for an island whose asymmetry parameter is 0.2.

I. ECCD Deposition Profile

Let us assume that the normalized profile of the current density driven by electron cyclotron waves in the island region (prior to equilibration around flux-surfaces) takes the form

$$J(x,\zeta) = \exp\left[-\frac{(x-d)^2}{2\,D^{\,2}}\right]\left[\frac{1+\cos(\zeta-\mathit{\Delta}\zeta)}{2}\right], \tag{103}$$

where D is the radial width of the profile, d the radial offset between the peak current and the rational surface, and $\mathit{\Delta}\zeta$ the angular offset between the peak current and the island O-point. Note that the profile is comparatively narrow in x, and comparatively wide in ζ, as is generally the case in experiments. It turns out that only the component of $J(x,\zeta)$ that is even in ζ contributes to the integral (91), so we can effectively write

$$J(x,\zeta) = \exp\left[-\frac{(x-d)^2}{2\,D^{\,2}}\right]\left(\frac{1+\cos\zeta\,\cos\mathit{\Delta}\zeta}{2}\right). \tag{104}$$

Let $\hat{D} = D/W$ and $\hat{d} = d/W$. Making use of Eq. (29), we obtain

$$J(\varsigma, Y,\zeta) = \exp\left[-\frac{(\varsigma\,Y+\delta\,\cos\zeta/\sqrt{8}-\hat{d})^2}{2\,\hat{D}^{\,2}}\right]\left(\frac{1+\cos\zeta\,\cos\mathit{\Delta}\zeta}{2}\right), \tag{105}$$

Let

$$J_O(\varsigma, Y,\zeta) = \exp\left[-\frac{(\varsigma\,Y+\delta\,\cos\zeta/\sqrt{8}-\hat{d})^2}{2\,\hat{D}^{\,2}}\right]\left(\frac{1+\cos\zeta}{2}\right), \tag{106}$$

$$J_X(\varsigma, Y,\zeta) = \exp\left[-\frac{(\varsigma\,Y+\delta\,\cos\zeta/\sqrt{8}-\hat{d})^2}{2\,\hat{D}^{\,2}}\right]\left(\frac{1-\cos\zeta}{2}\right), \tag{107}$$

$$J_{O+}(Y,\zeta) = \frac{J_O(1,Y,\zeta)+J_O(-1,Y,\zeta)}{2}, \tag{108}$$

$$J_{X+}(Y,\zeta) = \frac{J_X(1,Y,\zeta)+J_X(-1,Y,\zeta)}{2}. \tag{109}$$

It follows from Eq. (91) that

$$G_{\rm eccd}(\mathit{\Delta}\zeta) = G_{{\rm eccd}\,O}\left(\frac{1+\cos\mathit{\Delta}\zeta}{2}\right)+G_{{\rm eccd}\,X}\left(\frac{1-\cos\mathit{\Delta}\zeta}{2}\right), \tag{110}$$

$$G_{\mathrm{eccd}\,O} = -16\int_{-1}^{\infty}\frac{\langle J_{O+}\rangle\,\langle\cos\zeta\rangle}{\langle 1\rangle}\,d\Omega, \tag{111}$$

$$G_{\mathrm{eccd}\,X} = -16\int_{-1}^{\infty}\frac{\langle J_{X+}\rangle\,\langle\cos\zeta\rangle}{\langle 1\rangle}\,d\Omega. \tag{112}$$

Note that if there were no peaking of the current density profiles driven by electron cyclotron waves in the angular variable ζ (i.e., if the profile were independent of ζ) then the integral G_{eccd} would take the value $2\,G_{\mathrm{eccd}}(\Delta\zeta = \pi/2)$.

Figure 9 shows the integral G_{eccd} evaluated as a function of d/D for a thin island of width $W = 0.1\,D$ and asymmetry parameter $\delta = 0.5$. Now, it is clear from the modified Rutherford equation, (88), as well as from Fig. 8, that in order for ECCD to suppress an NTM to such an extent that the island width falls below the threshold value needed to trigger the mode, implying that the mode is completely stabilized, the integral G_{eccd} needs to be finite and positive in the limit as $W/D \to 0$. It is apparent from Fig. 8 that this is the case as long as $|d| \lesssim 2\,D$ and $\Delta\zeta \lesssim \pi/2$. In other words, successful stabilization is possible provided the radial offset of the peak current driven by electron cyclotron waves from the rational surface does not exceed twice the radial standard deviation of the current drive deposition profile, and as long as the angular offset of the peak current from the island O-point does not exceed $\pi/2$. The figure also indicates that for thin islands there is a considerable benefit to be had from peaking the deposition profile in ζ in the vicinity of the O-point (which, in practice, is achieved by modulating the electron cyclotron source such that it is only turned on the when the island O-point is directly in the line of fire), rather than having the profile independent of ζ (which, in practice, is achieved by not modulating the source).[38] (Here, we are assuming that the island chain is rotating, as is generally the case in experiments.)

Note that if the ECCD is optimal (i.e., $d = 0$ and $\Delta\zeta = 0$) then G_{eccd} attains a maximum value of 1.433 for an island whose asymmetry parameter is $\delta = 0.2$. Making use of Eqs. (88) and (100), as well as the information in Table I and Fig. 8, we deduce that the critical normalized peak driven current density at the $q = 3/2$ surface needed to stabilize a 3, 2 NTM with an asymmetry parameter of $\delta = 0.2$ is $J_{\max\,\mathrm{crit}} = 0.49$, which corresponds to an unnormalized peak current density of $j_{\max\,\mathrm{crit}} = 1.9 \times 10^5\,\mathrm{A/m^2}$. Likewise, the critical normalized peak driven current density at the $q = 2$ surface needed to stabilize a 2, 1

NTM with an asymmetry parameter of $\delta = 0.2$ is $J_{\max\,{\rm crit}} = 0.28$, which corresponds to an unnormalized peak current density of $j_{\max\,{\rm crit}} = 1.6\times 10^5\,{\rm A/m^2}$

Figures 10 and 11 show the integral $G_{\rm eccd}$ evaluated as a function of d/D for wide islands of width $W = 2\,D$ and $4\,D$, respectively, and asymmetry parameter $\delta = 0.5$. It can be seen that, as the island increases in width, the optimum radial location of the ECCD profile shifts inward from the rational surface.[38] This is indicative of the fact that the true target for ECCD is the island O-point (which is shifted inward from the rational surface a distance $W\,\delta/\sqrt{8}$) rather than the rational surface. It is again the case that the radial offset of the peak current from the island O-point needs to be less that twice the radial standard deviation of the current drive profile. Figures 10 and 11 also suggest that the benefit of modulating the electron cyclotron source is considerably reduced for wide islands compared to narrow islands.

V. GLOBAL PERTURBED ELECTRON TEMPERATURE

The asymptotic matching process consists of writing the NTM-modified electron temperature profile in the form

$$T_e(r,\theta,\phi) = T_{e\,0}(r) + \delta T_{e\,+} - \Psi_+\,\frac{q(r)}{r\,g(r)}\,\frac{T_{e\,0}'(r)\,\hat{\psi}_{m_l}(r)}{m_l - n\,q(r)}\,{\rm e}^{\,{\rm i}\,(m_l\,\theta - n\,\phi)}$$
$$- \Psi\sum_{j=1,J}^{m_j\neq m_l}\frac{q(r)}{r\,g(r)}\,\frac{T_{e\,0}'(r)\,\hat{\psi}_{m_j}(r)}{m_j - n\,q(r)}\,{\rm e}^{\,{\rm i}\,(m_j\,\theta - n\,\phi)} \tag{113}$$

in the segment of the outer region that lies outside the rational surface at which the NTM reconnects magnetic flux: i.e., $r > r_l + W$. Here, $T_{e\,0}'(r) = dT_{e\,0}/dr$. Likewise, the island-modified electron temperature profile takes the form

$$T_e(r,\theta,\phi) = T_{e\,0}(r) + \delta T_{e\,-} - \Psi_-\,\frac{q(r)}{r\,g(r)}\,\frac{T_{e\,0}'(r)\,\hat{\psi}_{m_l}(r)}{m_l - n\,q(r)}\,{\rm e}^{\,{\rm i}\,(m_l\,\theta - n\,\phi)}$$
$$- \Psi\sum_{j=1,J}^{m_j\neq m_l}\frac{q(r)}{r\,g(r)}\,\frac{T_{e\,0}'(r)\,\hat{\psi}_{m_j}(r)}{m_j - n\,q(r)}\,{\rm e}^{\,{\rm i}\,(m_j\,\theta - n\,\phi)} \tag{114}$$

in the segment of the outer region that lies inside the rational surface: i.e., $r < r_l - W$. Finally, the NTM-modified electron temperature profile takes the form

$$T_e(r,\theta,\phi) = T_{e\,l} + T_{e\,l}'\,W \sum_{\nu=0,\nu_{\rm max}} \delta T_\nu(x/W)\,{\rm e}^{\,{\rm i}\,\nu\,(m_l\,\theta-n\,\phi)}$$

$$- \Psi \sum_{j=1,J}^{m_j\neq m_l} \frac{q(r)}{r\,g(r)}\,\frac{T_{e\,0}'(r)\,\hat{\psi}_{m_j}(r)}{m_j - n\,q(r)}\,{\rm e}^{\,{\rm i}\,(m_j\,\theta-n\,\phi)} \tag{115}$$

in the inner region: i.e., $r_l - W < r < r_l + W$. Continuity of the solution at $r = r_l \pm W$ implies that

$$\delta T_{e\,+} = T_{e\,l}'\,W\,\delta T_0(1) + T_{e\,l}'\,W\,\delta T_{0\,+} - T_{e\,l}'\,W, \tag{116}$$

$$\delta T_{e\,-} = T_{e\,l}'\,W\,\delta T_0(-1) + T_{e\,l}'\,W\,\delta T_{0\,+} + T_{e\,l}'\,W, \tag{117}$$

$$\Psi_{+} = -T_{e\,l}'\,W\,\delta T_1(1)\left(\frac{r\,g}{q}\,\frac{m_l - n\,q}{T_{e\,0}'\,\hat{\psi}_{m_l}}\right)_{r_l+W}, \tag{118}$$

$$\Psi_{l-} = -T_{e\,l}'\,W\,\delta T_1(-1)\left(\frac{r\,g}{q}\,\frac{m_l - n\,q}{T_{e\,0}'\,\hat{\psi}_{m_l}}\right)_{r_l-W}. \tag{119}$$

Here, the NTM island width, W, is specified, and the reconnected magnetic flux, Ψ, and the island asymmetry parameter, δ, are then deduced from Eqs. (46) and (47), respectively. Moreover, m_l, n are, respectively, the poloidal and toroidal mode numbers of the NTM, r_l is the minor radius at which the NTM reconnects magnetic flux, $T_{e\,l} = T_{e\,0}(r_l)$, $T_{e\,l}' = T_{e\,0}'(r_l)$, $\delta T_{0\,+}$ is defined in Eq. (79), $\delta T_{e\,+}$ is the reduction in the equilibrium electron temperature profile outside the island rational surface, and $\delta T_{e\,-}$ is the corresponding reduction inside the rational surface. The asymptotic matching process assumes that the $\delta T_{\nu>1}$ are negligible at $r = r_l \pm W$. (See Fig. 6.)

Note that if we were to neglect the nonlinearly generated overtone harmonics of the m_l, n harmonic in the inner region then the temperature perturbation at a general toroidal angle, ϕ, could be expressed as a linear combination of the temperature perturbations at $\phi = 0$ and $\phi = \pi/(2\,n)$. However, the presence of the overtone harmonics spoils this scheme (because the harmonics have different toroidal mode numbers as well as different poloidal mode numbers). Hence, it is necessary to separately calculate the temperature perturbation at a large number of equally-spaced values of ϕ.

Table II shows various parameters derived from the asymptotic matching process for a 3, 2 and a 2, 1 NTM in the example plasma equilibrium pictured in Figs. 1 and 2. In both cases, we have chosen rather wide islands of width $W = 0.1\,a$ for ease of visualization. The asymmetry parameter for the 3, 2 mode is $\delta = 0.271$, whereas that for the 2, 1 mode is $\delta = 0.150$. This implies that both modes are characterized by radial asymmetric island chains in which the island O-points are shifted radially inward from the rational surfaces. Both modes are also (by design) characterized by rather small reductions in the equilibrium electron temperature outside the rational surface, and quite substantial reductions inside the rational surfaces.

Figure 12 shows the various harmonics of the 3, 2 and 2, 1 NTMs as functions of the flux-surface label r. Note that the overtone harmonics in the island regions are not shown in this figure. It can be seen that both NTMs consist of many coupled poloidal harmonics.

Figure 13 shows the perturbed electron temperatures associated with both NTMs at a particular toroidal angle. In this case, all harmonics are included in the calculation. (The allowed poloidal harmonics in the outer region have poloidal mode numbers in the range $m = -10$ to $m = +20$. The allowed overtone harmonics in the inner region are such that ν lies in the range 0 to 15.) It can be seen that the temperature perturbations have quite complicated structures. Nevertheless, when the temperature perturbations are added to the equilibrium electron temperature profile then flat spots are clearly visible in the vicinity of the NTM rational surfaces, as shown in Fig. 14.

VI. SUMMARY AND DISCUSSION

In this paper, we have demonstrated how the TJ toroidal tearing mode code can be used to make realistic predictions of the electron cyclotron emission (ECE) signals generated by neoclassical tearing modes (NTMs) in an ITER-like tokamak plasma equilibrium. (See Sect. II.) In the outer region, which comprises the bulk of the plasma, helical harmonics of the magnetic field with the same toroidal mode number as the NTM, but different poloidal mode numbers, are coupled together by the Shafranov shifts and shaping of the equilibrium magnetic flux-surfaces. (See Sect. III.) In the inner region, which is localized in the vicinity of the NTM rational surface, helical harmonics whose poloidal and toroidal mode numbers are in the same ratio as those of the NTM are coupled together nonlinearly to produce a radially asymmetric magnetic island chain. (See Sect. IV.) The solutions in the inner and outer regions are asymptotically matched to one another. (See Sect. V.) The asymptotic matching process determines the overall magnetic structure of the NTM, as well as the global perturbation to the electron temperature caused by the NTM.

Although an NTM can easily be detected using magnetic pickup coils located outside the plasma, this detection method is subject to substantial interference from other MHD modes, such as sawtooth oscillations and ELMs, and also does not determine the location of the NTM island chain. This is problematic because the cure for NTMs is to launch electron cyclotron waves into the plasma in such a manner as to drive a localized toroidal current in the vicinity of one of the O-points of the chain. In order to be effective, the location of the peak of the electron cyclotron current drive (ECCD) profile cannot miss the island O-point in major radius by more than two standard deviations of the radial width of the profile. (See Sect. V.) Fortunately, as is confirmed in this paper, ECE radiometry is capable of measuring the major radius of the island O-point, even when the width of the island chain is very much less than the minor radius of the plasma. (See Sect. **??**.) Moreover, this measurement is not subject to interference from sawtooth oscillations or ELMs, because such modes do not produce flat spots in the electron temperature profile. However, the accuracy of the ECE diagnostic is limited by the fact that the signal is downshifted and broadened in frequency due to the relativistic mass increase of the emitting electrons. It is clear, from the calculations in this paper, that the radial location of the O-point deduced by an ECE diagnostic needs to be corrected for the relativistic downshifting, which causes the inferred location to shift outward in major radius from the rational surface, as well as the fact that the island O-point is shifted inward from the rational surface. An example of such a correction is shown in Fig. **??**.

The type of calculation described in this paper can be performed sufficiently rapidly that it would be possible to generate a large synthetic ECE data-set that could be used as the input to a machine-learning algorithm. In this manner, it would be possible to train a neural network to detect an NTM magnetic island chain using experimental ECE data when the chain is still relatively narrow, as well as to accurately determine the location of one of the island O-points.

ACKNOWLEDGEMENTS

This research was directly funded by the U.S. Department of Energy, Office of Science, Office of Fusion Energy Sciences, under contract DE-SC0021156. The author acknowledges useful and informative discussions with W.L. Rowan, J.P. Ziegel, and Max Austin.

DATA AVAILABILITY STATEMENT

The digital data used in the figures in this paper can be obtained from the author upon reasonable request. The TJ code is freely available at `https://github.com/rfitzp/TJ`.

Appendix A: Electron Cyclotron Emission

1. Introduction

This appendix reviews the theory of electron cyclotron emission (ECE) from ITER-like tokamak plasmas, and is based on the analysis of Bornatici et al.,[63] which is ultimately based on the work of Bekefi.[64] It is currently planned to use 1st harmonic O-mode and 2nd harmonic X-mode ECE emission to detect NTMs in ITER.[33] Here, O-mode and X-mode refer to electromagnetic waves that propagate perpendicular to the equilibrium magnetic field, with the former polarized such that the electric component of the wave is parallel to the magnetic field, and the latter such that it is perpendicular.[61] First harmonic refers to emission whose frequency matches the local cyclotron frequency at the emission site, whereas 2nd harmonic corresponds to emission at twice the cyclotron frequency.[61]

2. Orderings

Our analysis premised on three main assumptions.

Our first assumption is that the ECE emission lies in the so-called *relativistic regime*, in which the broadening of the emission is predominately due to the relativistic mass increase of emitting electrons, as opposed to the Doppler effect. The emission is in the relativistic regime provided that

$$|N\,\cos\vartheta| \ll \frac{v_t}{c}, \tag{A1}$$

where

$$v_t = \left(\frac{T_e}{m_e}\right)^{1/2}. \tag{A2}$$

Here, N is the refractive index, ϑ the angle subtended between the ECE wave-vector and the equilibrium magnetic field, T_e the equilibrium electron temperature, m_e the electron rest mass, c the velocity of light in vacuum, and v_t the electron thermal speed. All quantities are evaluated at the ECE emission site, which invariably lies close to the point at which the cyclotron resonance condition

$$\omega = j\,\omega_c \tag{A3}$$

is satisfied, where

$$\omega_c = \frac{e\,B}{m_e}. \tag{A4}$$

Here, ω is the angular frequency of the emitted radiation, e is the magnitude of the electron charge, B is the equilibrium magnetic field-strength at the emission site, and ω_c the local cyclotron frequency. Moreover, $j = 1$ for 1st harmonic emission, whereas $j = 2$ for 2nd harmonic emission. The constraint (A1) is easily satisfied because we are assuming that $\vartheta = \pi/2$.

Our second assumption is that the ECE emission lies in the so-called *small gyro-radius limit*, in which the gyro-radii of the emitting electrons are much smaller than the wavelength of the emitted radiation. This limit holds provided that

$$j^{\,2}\,N^2\left(\frac{v_t}{c}\right)^2 = 1.96\times 10^{-3}\,j^{\,2}\,N\,T_e(\text{keV}) \ll 1, \tag{A5}$$

which is easily satisfied in ITER-like plasmas.

Our final assumption is that the ECE emission lies in the so-called *tenuous plasma limit*, in which

$$\left(\frac{\omega_p}{\omega_c}\right)^2 = 10.3\,\frac{n_e(10^{20}\,\text{m}^{-3})}{B^2(\text{T})} \ll 1, \tag{A6}$$

where

$$\omega_p = \left(\frac{n_e\,e^2}{\epsilon_0\,m_e}\right)^{1/2} \tag{A7}$$

is the electron plasma frequency at the emission site, whereas n_e is the local electron number density. The constraint (A6) is (barely) satisfied in ITER when operating at the full designed toroidal magnetic field of $B_\phi = 5.3\,\mathrm{T}$.

3. ECE Signal

The ECE signal generated by an NTM in ITER will be measured on a horizontal chord that passes through the magnetic axis of the plasma. See Fig. 1. This chord is such that Z and ϕ are constant on it, whereas the major radius, R, varies. Such a chord corresponds to a possible path of ECE because the perpendicular gradient of the plasma refractive index is zero along the chord due to the assumed up-down symmetric nature of the plasma equilibrium. The fact that ϕ is constant along the chord implies that $\vartheta \simeq \pi/2$, so that Doppler broadening of the ECE signal is eliminated.[33,39]

In thermal equilibrium, assuming that the plasma is optically thick to ECE radiation [see Fig. 16) and (17)], the so-called *radiation temperature* measured by the ECE diagnostic is related to the *radiance*, $I(\omega)$, of the ECE signal as follows:[63]

$$T_{\rm rad}(\omega) = \frac{8\pi^3\,c^2\,I(\omega)}{\omega^2}. \tag{A8}$$

Here,

$$I(\omega) = \frac{\omega^2}{8\pi^3\,c^2}\int_{R_{\rm hfs}}^{R_{\rm lfs}} G(\omega, R)\,dR, \tag{A9}$$

where $G(\omega, R)$ is the so-called *emissivity function.* Moreover, R is the major radius of a location on the ECE measurement chord, $R_{\rm hfs}$ is the major radius of the plasma boundary on the high-field side (i.e., the inner side) of the chord, whereas $R_{\rm lfs}$ is the major radius of the plasma boundary on the low-field side (i.e., the outer side).

The emissivity function takes the form[63]

$$G(\omega, R) = T_e(R)\,\alpha(\omega, R)\,\exp\left[-\tau(\omega, R)\right], \tag{A10}$$

where

$$\tau(\omega, R) = \int_R^{R_{\rm lfs}} \alpha(\omega, R')\, dR' \tag{A11}$$

is the dimensionless *optical depth.* Here, $T_e(R)$ is the electron temperature on the measurement chord (including the perturbation due to the NTM), whereas $\alpha(\omega, R)$ is the so-called *absorption coefficient.*

In ITER-like plasmas, it is an excellent approximation to write

$$B(R) = \frac{B_0\, R_0}{R}, \tag{A12}$$

where B_0 is the toroidal magnetic field-strength at the magnetic axis. It follows that

$$\omega_c(R) = \frac{\omega_{c\,0}\, R_0}{R}, \tag{A13}$$

where

$$\omega_{c\,0} = \frac{e\, B_0}{m_e} \tag{A14}$$

is the cyclotron frequency on the magnetic axis. Thus, we can use the local cyclotron frequency, $\omega_c(R)$, as a proxy for major radius, R, along the measurement chord.

Equations (A8)–(A11) and (A13) can be combined to give

$$T_{\rm rad}(\omega) = \int_{\omega_{c\,\rm lfs}}^{\omega_{c\,\rm hfs}} T_e(\omega_c)\, H(\omega, \omega_c)\, d\omega_c, \tag{A15}$$

where

$$H(\omega, \omega_c) = \tau_0\, \frac{\hat{\alpha}(\omega, \omega_c)}{\omega_c}\, \exp\left[-\tau(\omega, \omega_c)\right], \tag{A16}$$

$$\tau(\omega, \omega_c) = \tau_0 \int_{\omega_{c\,\rm lfs}}^{\omega_c} \frac{\hat{\alpha}(\omega, \omega_c')}{\omega_c'}\, d\omega_c', \tag{A17}$$

Here, $\omega_{c\,\rm lfs} = \omega_{c\,0}\, R_0/R_{\rm lfs}$, $\omega_{c\,\rm hfs} = \omega_{c\,0}\, R_0/R_{\rm hfs}$,

$$\tau_0 = \frac{\omega_{c\,0}\, R_0}{c} = 5.97 \times 10^2\, R_0({\rm m})\, B_0({\rm T}) \tag{A18}$$

is the dimensionless ratio of the major radius of the plasma to the typical wavelength of the ECE, and $\hat{\alpha}(\omega, \omega_c) = (c/\omega_c)\, \alpha(\omega, \omega_c)$ is a convenient dimensionless form of the absorption coefficient.

It is clear from Eq. (A15) that the radiation temperature measured by the ECE diagnostic, $T_{\rm rad}(\omega)$, is a convolution of the true electron temperature, $T_e(\omega)$, with the *spectral convolution function*, $H(\omega,\omega_c)$. The convolution function specifies the downshifting and broadening (in frequency) of the ECE signal due to the relativistic mass increase of the emitting electrons.

It is convenient to define

$$R_\omega(\omega) = \frac{j\,\omega_{c\,0}\,R_0}{\omega}, \tag{A19}$$

as the major radius from which jth harmonic ECE would originate in the absence of the aforementioned downshifting and broadening of the signal. Thus, we can also write

$$T_{\rm rad}(R_\omega) = \int_{R_{\rm lfs}}^{R_{\rm hfs}} T_e(R)\,F(R_\omega,R)\,dR, \tag{A20}$$

where

$$F(R_\omega,R) = \frac{\omega_{c\,0}\,R_0\,G(\omega,\omega_c)}{R^2}, \tag{A21}$$

According to Eq. (A20), the electron temperature profile along the measurement chord that is inferred from the ECE diagnostic, $T_{\rm rad}(R_\omega)$, is the convolution of the true temperature profile, $T_e(R)$, with the *spatial convolution function*, $F(R_\omega,R)$.

4. First Harmonic O-Mode Absorption Coefficient

The dimensionless absorption coefficient for 1st harmonic O-mode ECE is [63]

$$\hat{\alpha}_1^{(O)} = \frac{N\,(1/2)\,(\omega_p/\omega_c)^2\,[-F_{7/2}''(z_1)]}{1+(1/2)\,(\omega_p/\omega_c)^2\,F_{7/2}'(z_1)}, \tag{A22}$$

where

$$N^{\,2} = \frac{1-(\omega_p/\omega_c)^2}{1+(1/2)\,(\omega_p/\omega_c)^2\,F_{7/2}'(z_1)}, \tag{A23}$$

and

$$z_1 = \left(\frac{c}{v_t}\right)^2\left(1-\frac{\omega_c}{\omega}\right). \tag{A24}$$

Here, N is the real part of the plasma refractive index, and ω_p and v_t are evaluated at $z_1=0$. Moreover, $F_{7/2}'(z)$ and $F_{7/2}''(z)$ are, respectively, the real and imaginary parts of the function [63]

$$F_{7/2}(z) = \frac{8}{15}\left[z^2-\frac{z}{2}+\frac{3}{4}-\pi^{1/2}\,z^{5/2}\,w({\rm i}\sqrt{z})\right]. \tag{A25}$$

Here,

$$w(\xi) = \exp(-\xi^2)\,\mathrm{erfc}(-\mathrm{i}\,\xi) \tag{A26}$$

is a so-called *Faddeeva function* (alternatively known as a Kramp function), and erfc(z) is the complementary error function.[65]

Figure 15 shows the real and imaginary parts of the function $F_{7/2}(z)$. It is clear from Eq. (A22), (A24), and the figure, that 1st harmonic O-mode ECE is absorbed by the plasma in a range of frequencies that lie slightly above the cyclotron frequency, ω_c. This corresponds to a range of major radii that lies just inside the location of the 1st harmonic cyclotron resonance.

Figure 16 shows the normalized absorption coefficient, optical depth, spectral convolution function, and spatial convolution function for 1st harmonic O-mode ECE in a typical ITER-like plasma. It can be seen that the saturated optical depth is quite large (about 80), and that the full width of the spatial convolution function is about 7 cm. The dotted curve in the bottom right panel of the figure shows a Gaussian fit to the spatial convolution function. The fit is very good, indicating that the convolution function can be represented as

$$F_1^{(O)}(R_\omega, R) = \frac{1}{\sqrt{2\pi}\,\sigma_1^{(O)}}\,\exp\left(-\frac{\left[R - R_\omega + \delta_1^{(O)}\right]^2}{2\left[\sigma_1^{(O)}\right]^2}\right) \tag{A27}$$

Note that the fit to the function is characterized by just two parameters: the standard deviation, $\sigma_1^{(O)}$, and the inward shift of function peak from the cyclotron resonance, $\delta_1^{(O)}$.

5. Second Harmonic X-Mode Absorption Coefficient

The dimensionless absorption coefficient for 2nd harmonic X-mode ECE is[63]

$$\hat{\alpha}_2^{(X)} = \frac{N\,(\omega_p/\omega_c)^2\,(1+a_2)^2\,[-F''_{7/2}(z_2)]}{1 + (1/2)\,(\omega_p/\omega_c)^2\,(1+a_2)^2\,F'_{7/2}(z_2)}, \tag{A28}$$

where

$$a_2 = \frac{(1/6)\,(\omega_p/\omega_c)^2\left[1 + 3\,N^2\,F'_{7/2}(z_2)\right]}{1 - (1/3)\,(\omega_p/\omega_c)^2\left[1 + (3/2)\,N^2\,F'_{7/2}(z_2)\right]}, \tag{A29}$$

$$N^2 = N_c^2\left[1-(b+a\,N_c^2)\right], \tag{A30}$$

$$a = -\frac{(1/2)\,(\omega_p/\omega_c)^2\,F'_{7/2}(z_2)}{1-(1/3)\,(\omega_p/\omega_c)^2}, \tag{A31}$$

$$b = -2\left[1-\frac{1}{3}\left(\frac{\omega_p}{\omega_c}\right)^2\right]a, \tag{A32}$$

$$N_c^2 = 1-\frac{(1/6)\,(\omega_p/\omega_c)^2\,[1-(1/4)\,(\omega_p/\omega_c)^2]}{1-(1/3)\,(\omega_p/\omega_c)^2}, \tag{A33}$$

$$z_2 = \left(\frac{c}{v_t}\right)^2\left(1-\frac{2\,\omega_c}{\omega}\right). \tag{A34}$$

Here, v_t and ω_p are evaluated at $z_2 = 0$. Moreover, the parameters a, b, and N_c have been calculated assuming that $\omega = 2\,\omega_c$.

Figure 17 shows the normalized absorption coefficient, optical depth, spectral convolution function, and spatial convolution function for 2nd harmonic O-mode ECE in a typical ITER-like plasma. It can be seen that the saturated optical depth is very large (about 200), and that the full width of the spatial convolution function is about 5 cm. The dotted curve in the bottom right panel of the figure shows a Gaussian fit to the spatial convolution function. The fit is very good, indicating that the convolution function can be represented as

$$F_2^{(X)}(R_\omega, R) = \frac{1}{\sqrt{2\pi}\,\sigma_2^{(X)}}\,\exp\left(-\frac{\left[R-R_\omega+\delta_2^{(X)}\right]^2}{2\left[\sigma_2^{(X)}\right]^2}\right) \tag{A35}$$

Note that the fit to the function is characterized by just two parameters: the standard deviation, $\sigma_2^{(X)}$, and the inward shift of function peak from the cyclotron resonance, $\delta_2^{(X)}$.

---

[1] T.C. Hender, J.C Wesley, J. Bialek, A. Bondeson, A.H. Boozer, R.J. Buttery, A. Garofalo, T.P Goodman, R.S. Granetz, Y. Gribov, O. Gruber, M. Gryaznevich, et al., Nucl. Fusion **47**, S128 (2007).

[2] J.A. Wesson, *Tokamaks*, 4th Ed., (Oxford University Press, Oxford UK, 2011).

[3] J.A. Wesson, R.D. Gill, M. Hugon, F.C. Schüller, J.A. Snipes, D.J. Ward, D.V. Bartlett, D.J. Campbell, P.A. Duperrex, A.W. Edwards, R.S. Granetz, N.A.O. Gottardi, T.C Hender,

E. Lazzaro, P.J.. Lomas, N. Lopes Cardozo, K.F. Mast, M.F.F. Nave, N.A. Salmon, P. Smeulders, P.R. Thomas, B.J.D. Tubbing, M.F. Turner and A. Weller, Nucl. Fusion **29** 641 (1989).

[4] H.P. Furth, J. Killeen and M.N. Rosenbluth, Phys. Fluids **6**, 459 (1963).

[5] P.H. Rutherford, Phys. Fluids **16**, 1906 (1973).

[6] R.D. Hazeltine and J.D. Meiss, Phys. Reports **121**, 1 (1985).

[7] R. Fitzpatrick, Phys. Plasmas **2**, 825 (1995).

[8] R.J. Bickerton, J.W. Connor and J.B. Taylor, Nat. Phys. Sci. **229**, 110 (1971).

[9] Z. Chang, E.D. Fredrickson, S.H. Batha, M.G. Bell, R.V. Budny, F.M. Levinton, K.M. McGuire, G. Taylor, M.C. Zarnstorff and the TFTR Group, Phys. Plasmas **5**, 1076 (1998).

[10] C.C. Hegna, Phys. Plasmas **5**, 1767 (1998).

[11] R.J. Buttery, S. Günter, G. Giruzzi, T.C. Hender, D. Howell, G. Huysmans, R.J. La Haye, M. Maraschek, H. Reimerdes, O. Sauter, C.D. Warrick, H.R. Wilson and H. Zohm, Plasma Phys. Control. Fusion **42**, B61 (2000).

[12] H.R. Wilson, Fusion Science and Technology **61**, 113 (2012).

[13] R.J. La Haye, Phys. Plasmas **13**, 055501 (2006).

[14] M. Maraschek, Nucl. Fusion **52**, 074007 (2007).

[15] P.C. de Vries, M.F. Johnson, B. Alper, P. Buratti, T.C. Hender, H.R. Koslowski, V. Riccardo and JET-EFDA Contributors, Nucl. Fusion **51**, 053018 (2011).

[16] O. Sauter, E. Westerhof, M.L. Mayoral, B. Alper, P.A. Belo, R.J. Buttery, A. Gondhalekar, T. Hellsten, T.C. Hender, D.F. Howell, T. Johnson, P. Lamalle, M.J. Mantsinen, F. Milani, M.F.F. Nave, F. Nguyen, A.L. Pecquet, S.D. Pinches, S. Podda and J. Rapp, Phys. Rev. Lett. **88**, 105001 (2002).

[17] R.J. La Haye, C. Chrystal, E.J. Strait, J.D. Callen, C.C. Hegna, E.C. Howell, M. Okabayashi and R.S. Wilcox, Nucl. Fusion **62**, 056017 (2022).

[18] R. Fitzpatrick, R. Maingi, J.-K. Park and S. Sabbagh, Phys. Plasmas **30**, 072505 (2023).

[19] E.D. Fredrickson, Phys. Plasmas **9**, 548 (2002).

[20] H. Zohm, Phys. Plasmas **4**, 3433 (1997).

[21] R. Prater, Phys. Plasmas **13**, 055501 (2006).

[22] G. Gantenbein, H. Zohm, G. Giruzzi, S. Günter, F. Leuterer, M. Maraschek, J. Meskat, Q. Yu, ASDEX Upgrade Team and ECRH-Group (AUG), Phys. Rev. Lett. **85**, 1242 (2000).

[23] A. Isayama, Y. Kamada, S. Ide, K. Hamamatsu, T. Oikawa, T. Suzuki, Y. Neyatani, T. Ozeki, Y. Ikeda, K. Kajiwara and the JT-60 team, Plasma Phys. Control. Fusion **42**, L37 (2000).

[24] R.J. La Haye, S. Günter, D.A. Humphreys, J. Lohr, T.C. Luce, M.E. Maraschek, C.C. Petty, R. Prater, J.T. Scoville and E.J. Strait, Phys. Plasmas **9**, 2051 (2002).

[25] M. Kong, T.C. Blanken, F. Felici, C. Galperti, E. Maljaars, O. Sauter, T. Vu, F. Carpanese, A. Merle, J.-M. Moret, F. Pesamosca, E. Poli, M. Reich, A.A. Teplukhina, the TCV Team and the EUROfusion MST Team, Nucl. Fusion **59**, 076035 (2019).

[26] J.-C. Li, J.-Q. Dong, X.-Q. Ji and Y.-J. Hu, Chinese Phys. B **30**, 075203 (2021).

[27] Y. Zhang, X.J. Wang, F. Hong, W. Zhang, H.D. Xu, T.H. Shi, E.Z. Li, Q. Ma, H.L. Zhao, S.X. Wang, Y.Q. Chu, H.Q. Liu, Y.W. Sun, X.D. Zhang, Q. Yu, J.P. Qian, X.Z. Gong, J.S. Hu, K. Lu, Y.T. Song and the EAST Team, Nucl. Fusion **64**, 076016 (2024).

[28] Y.S. Park, M.H. Woo, S.A. Sabbagh, H.S. Han, B.H. Park, J.S. Kang and H.S. Kim, Plasma Phys. Control. Fusion **66**, 125013 (2024).

[29] H. van den Brand, M.R. de Baar, N.J. Lopes-Cardozo and E. Westerhof, Nucl. Fusion **53**, 013005 (2013).

[30] M. Bornatici, R. Cano, O. de Barbieri and F. Englemann, Nucl. Fusion **23**, 1153 (1983).

[31] M. Bornatici, F. Englemann and U. Ruffina, Sov. J. Quantum Electron. **13**, 68 (1983).

[32] J. Berrino, E. Lazzaro, S. Cirant, G. D'Antona, F. Gandini, E. Minardi and G. Granuci, Nucl. Fusion **45**, 1350 (2005).

[33] J.P. Ziegel, W.L. Rowan and F.L. Waelbroeck, Nucl. Fusion **64**, 126032 (2024).

[34] J.W. Connor, R.J. Hastie and J.B. Taylor, Phys. Fluids B **3**, 1539 (1991).

[35] J.W. Connor, S.C. Cowley, R.J. Hastie, T.C. Hender, A. Hood and T.J. Martin, Phys. Fluids

31, 577 (1988).

[36] R. Fitzpatrick, R.J. Hastie, T.J. Martin and C.M. Roach, Nucl. Fusion **33**, 1533 (1993).

[37] J.P. Meskat, H. Zohm, G. Gantenbein, S. Günter, M. Maraschek, W. Suttrop, Q. Yu and ASDEX Upgrade Team, Plasma Phys. Control. Fusion **43** , 1325 (2001).

[38] D. De Lazzari and F. Westerhof, Plasma Phys. Control. Fusion **53**, 035020 (2011).

[39] J.P. Ziegel, W.L. Rowan and F.L. Waelbroeck, Rev. Sci. Instrum. **95**, 073510 (2024).

[40] A. Pletzer and R.L. Dewar, J. Plasma Physics **45**, 427 (1991).

[41] A.H. Glasser, Z.R. Wang and J.-K. Park, Phys. Plasmas **23**, 112506 (2016).

[42] A.S. Glasser, E. Kolemen and A.H. Glasser, Phys. Plasmas **25**, 032507 (2018).

[43] A.S. Glasser and E. Koleman, Phys. Plasmas **25**, 082502 (2018).

[44] R. Fitzpatrick, Phys. Plasmas **31**, 102507 (2024).

[45] R. Fitzpatrick, *Investigation of Tearing Mode Stability Near Ideal Stability Boundaries Via Asymptotic Matching Techniques*, submitted to Physics of Plasmas (2025).

[46] R. Fitzpatrick, Phys. Plasmas **23**, 122502 (2016).

[47] R. Fitzpatrick, Phys. Plasmas **31**, 082505 (2024).

[48] C. Mercier, Nucl. Fusion **1**, 47 (1960).

[49] A.H. Glasser, J.M. Greene and J.L. Johnson, Phys. Fluids **18**, 875 (1975).

[50] A.H. Glasser, J.M. Greene and J.L. Johnson, Phys. Fluids **19**, 567 (1976).

[51] Z. Chang and J.D. Callen, Nucl. Fusion **30**, 219 (1990).

[52] R.B. White, D.A. Gates and D.P. Brennan, Phys. Plasmas **22**, 022514 (2015).

[53] F.L. Waelbroeck, Phys. Fluids B **1**, 2373 (1989).

[54] D. Brouwer and G.M. Clemance, *Methods of Celestial Mechanics*, (Academic Press, New York NY, 1961). Ch. II.

[55] I.S. Gradshteyn and I.M. Ryzhik, *Table of Integrals, Series, and Products*, Corrected and Enlarged Edition, (Academic Press, New York NY, 1980). Sect. 3.719.

[56] M.N. Rosenbluth, R.D. Hazeltine and F.L. Hinton, Phys. Fluids **15**, 116 (1972).

[57] R. Fitzpatrick, *Tearing Mode Dynamics in Tokamak Plasmas*, (IOP Publishing, Bristol UK, 2023).

[58] J.W.Connor, F.L.Waelbroeck and H.R. Wilson, Phys. Plasmas **8**, 2835 (2001).

[59] R. Carrera, R.D. Hazeltine and M. Kotschenreuther, Phys. Fluids **29**, 899 (1986).

[60] R.D. Hazeltine, M. Kotschenreuther and P.G. Morrison, Phys. Fluids **28**, 294 (1985).

[61] R. Fitzpatrick, *Plasma Physics: An Introduction*, 2nd Ed., (CRC Press, Boca Raton FL, 2023).

[62] R. Fitzpatrick, *Thermodynamics and Statistical Mechanics*, (World Scientific, Singapore, 2020).

[63] M. Bornatici, R. Cano, O. De Barbieri and F. Engelmann, Nucl. Fusion **23**, 1153 (1983).

[64] G. Bekefi, *Radiation Processes in Plasmas*, (John Wiley & Sons, New York NY, 1966).

[65] M. Abramowitz and I.A. Stegun, *Handbook of Mathematical Functions.* (Dover, New York NY, 1965.) Ch. 7.

m	n	$\hat{r}_l$	L_s	E_{ll}	$\varDelta_{l\,\mathrm{crit}}$	$\hat{\beta}$	α_b	α_c
3	2	0.6195	1.756	1.709	17.56	0.05521	2.588	0.5816
2	1	0.7874	1.201	13.66	36.45	0.03034	3.061	1.000

TABLE I. The poloidal mode number, toroidal mode number, normalized minor radius, normalized magnetic shear-length, linear tearing stability index, critical linear tearing stability index, normalized electron pressure, bootstrap parameter, and curvature parameter, respectively, at the 3, 2 and the 2, 1 rational surfaces of the example plasma equilibrium pictured in Figs. 1 and 2.

m	n	W/a	$\varPsi$	δ	$\delta T_{e\,+}$(eV)	$\delta T_{e\,-}$(eV)
3	2	0.1	4.89×10^{-4}	0.271	-0.977	-597
2	1	0.1	3.48×10^{-4}	0.150	-0.069	-476

TABLE II. The poloidal mode number, toroidal mode number, island width, normalized reconnected flux, island asymmetry parameter, equilibrium electron temperature reduction outside the rational surface, and equilibrium electron temperature reduction inside the rational surface, respectively, for a 3, 2 and a 2, 1 NTM in the example plasma equilibrium pictured in Figs. 1 and 2.

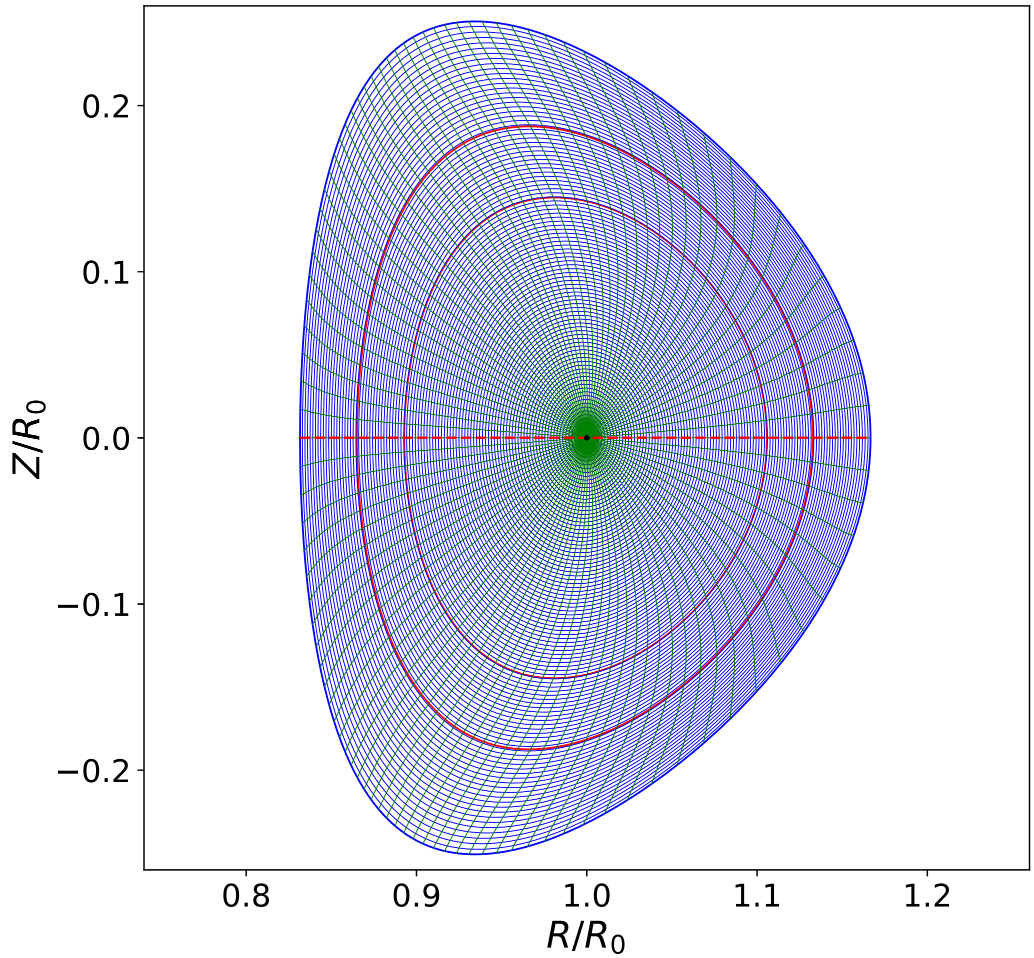

FIG. 1. The blue and green curves show surfaces of constant r and θ, respectively, for an ITER-like example plasma equilibrium characterized by $B_0 = 5.3$ T, $R_0 = 6.2$ m, $a = 0.2$, $H_2(1) = 1.0$, and $H_3(1) = 0.5$. The red curves show the locations of the $q = 3/2$ and $q = 2$ surfaces. The black dot shows the location of the magnetic axis. The dashed red line shows the location of the ECE measurement chord.

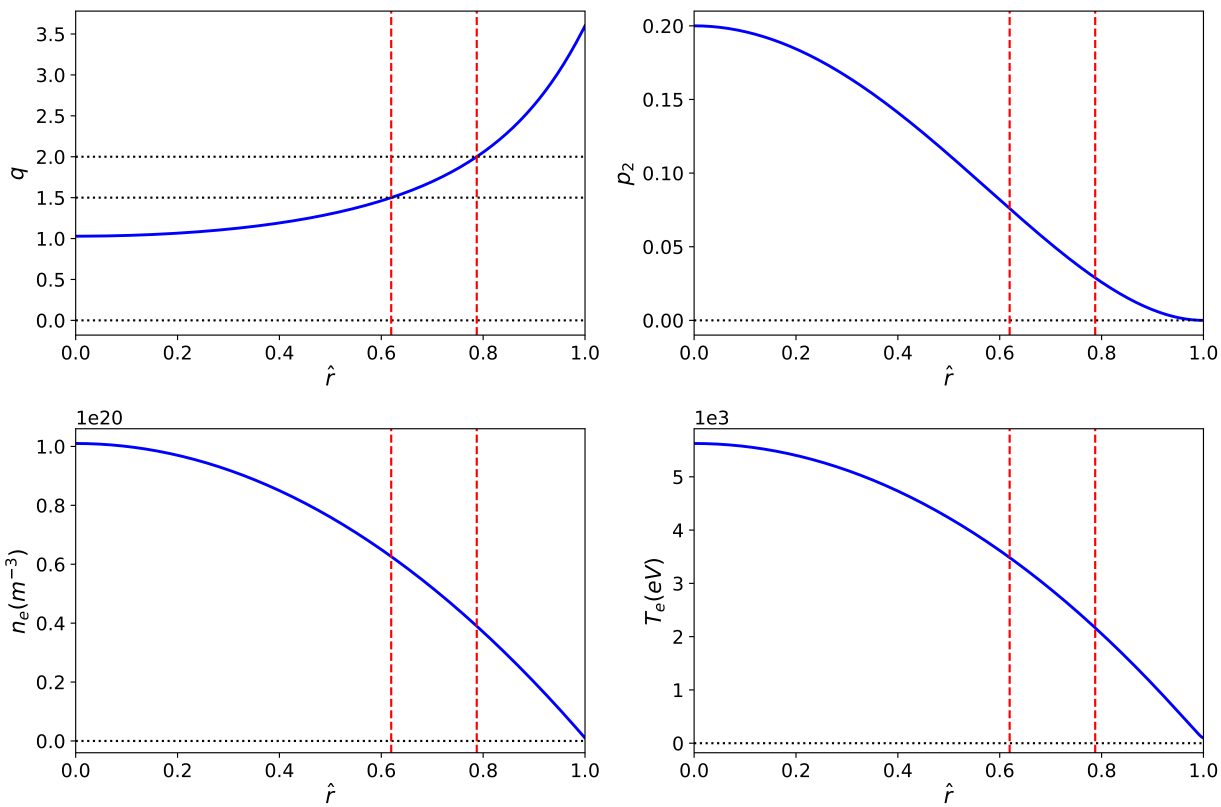

FIG. 2. The safety-factor, normalized pressure, electron number density, and electron temperature profiles for the example equilibrium pictured in Fig. 1. The vertical red lines show the locations of the $q = 3/2$ and $q = 2$ surfaces.

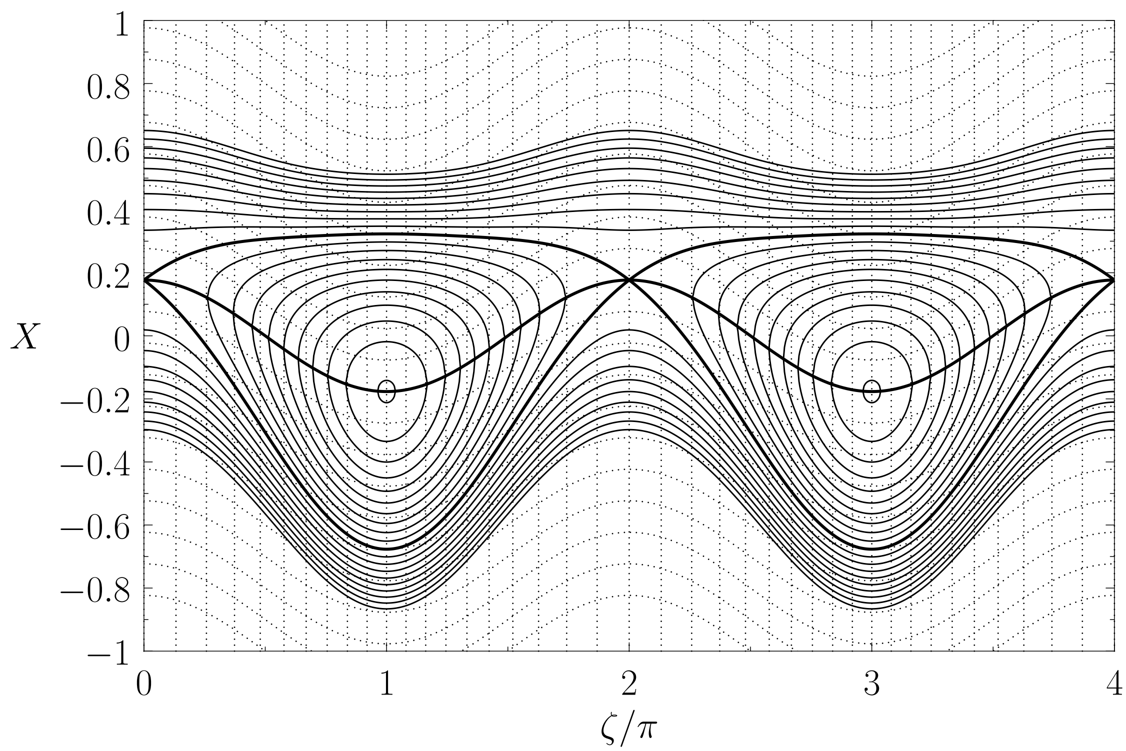

FIG. 3. The thin solid curves show the contours of $\Omega(X, \zeta)$ evaluated for $\delta = 0.5$. The thick solid lines show the magnetic separatrix (upper and lower curves) and the contour $Y = 0$ (middle curve). The curved dotted lines show equally-spaced contours of Y, whereas the vertical dotted lines show equally-spaced contours of ξ. (Reproduced, with permission, from Ref. 46.)

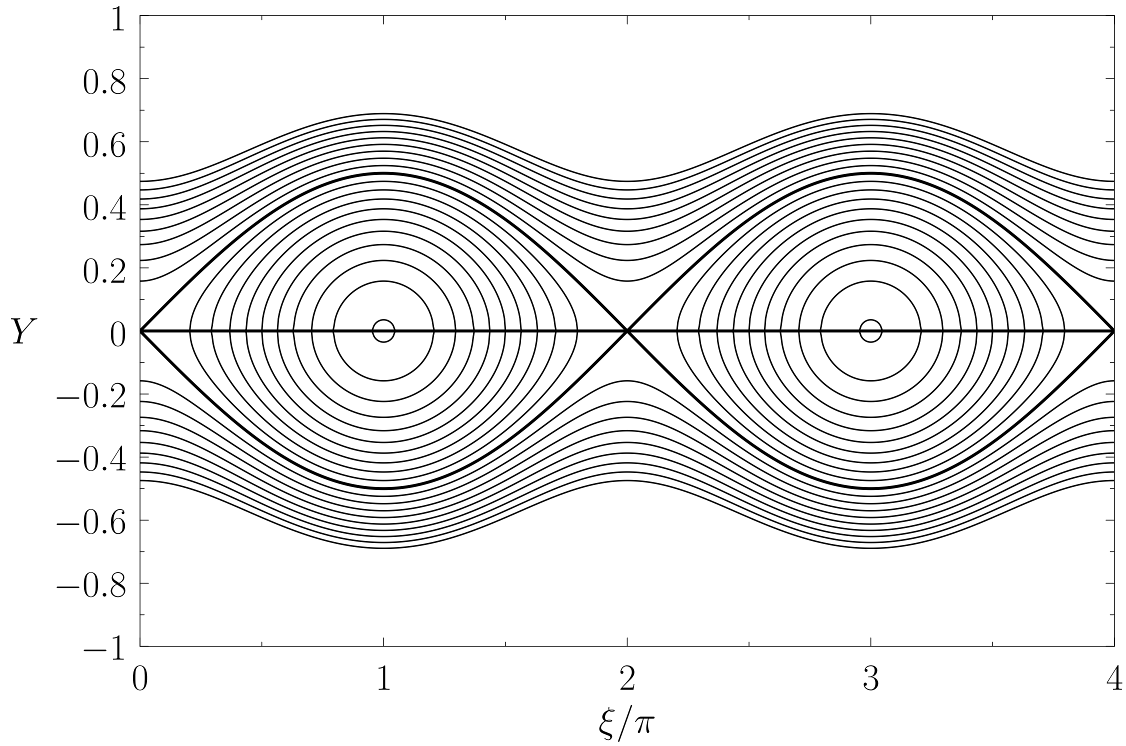

FIG. 4. The thin solid curves show the contours of $\Omega(Y, \xi)$ evaluated for $\delta = 0.5$. The thick solid lines show the magnetic separatrix (upper and lower curves) and the contour $Y = 0$ (middle curve). (Reproduced, with permission, from Ref. 46.)

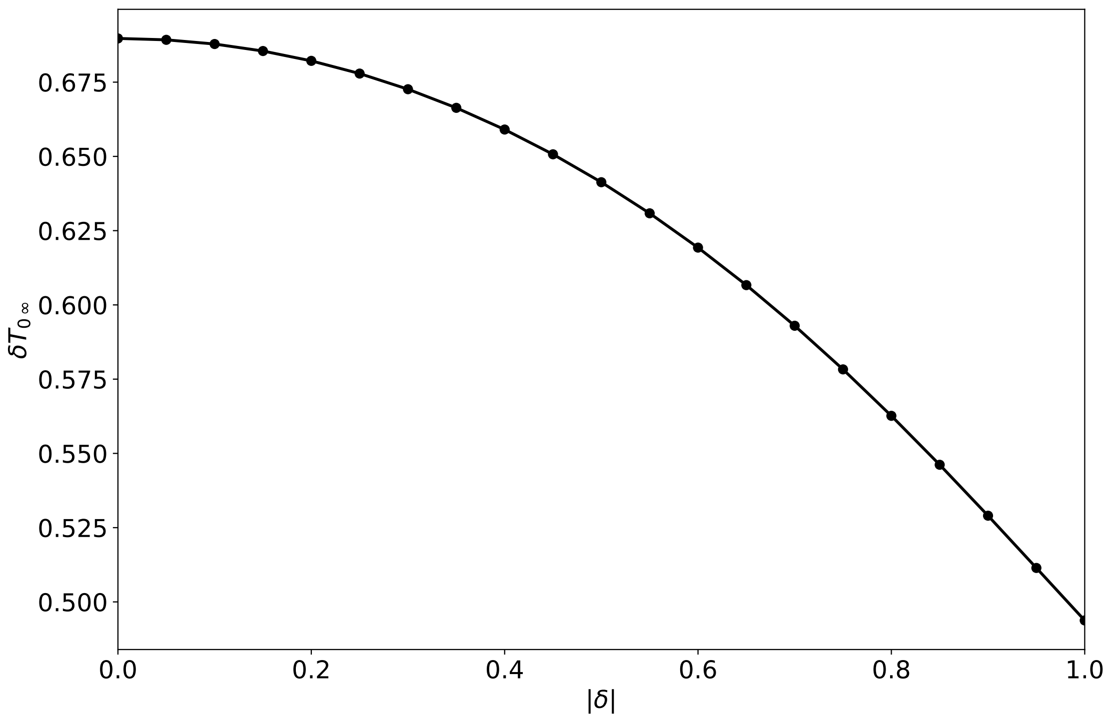

FIG. 5. The island temperature flattening parameter, $T_{0\,\infty}$, plotted as a function of the modulus of the island asymmetry parameter, $|\delta|$.

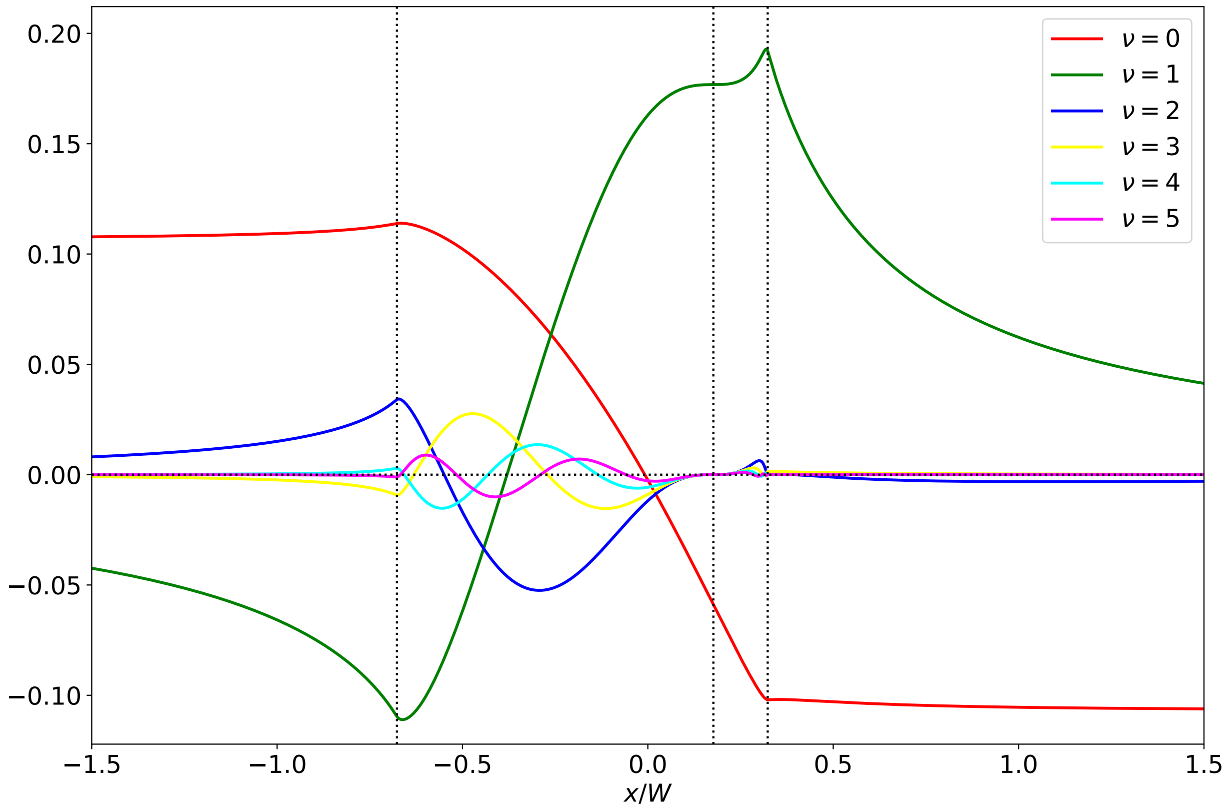

FIG. 6. The helical harmonics of the normalized electron temperature in the inner region, $\delta T_\nu(x/W)$, calculated for an asymmetric magnetic island characterized by $\delta = 0.5$. The curve labelled 0 actually shows $[\delta T_0(x/W) - x/W]/3$, whereas the curve labelled 1 actually shows $\delta T_1(x/W) + \delta/\sqrt{8}$. The vertical dotted lines show the locations of the inner limit of the magnetic separatrix, the island X-point, and the outer limit of the magnetic separatrix, in order from the left to the right.

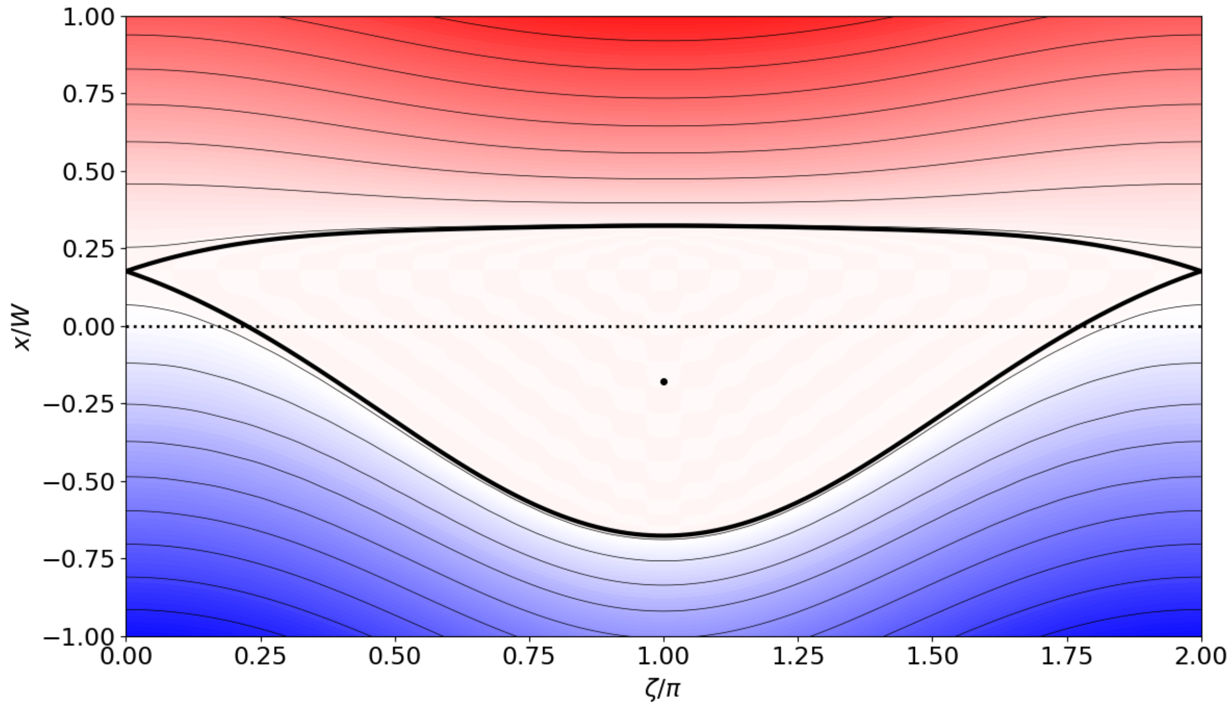

FIG. 7. Contours of the normalized electron temperature profile, $\tilde{T}(x/W, \zeta)$, in the vicinity of an asymmetric magnetic island characterized by $\delta = 0.5$. The thick solid line shows the magnetic separatrix, the dotted line shows the rational surface, and the black dot shows the island O-point.

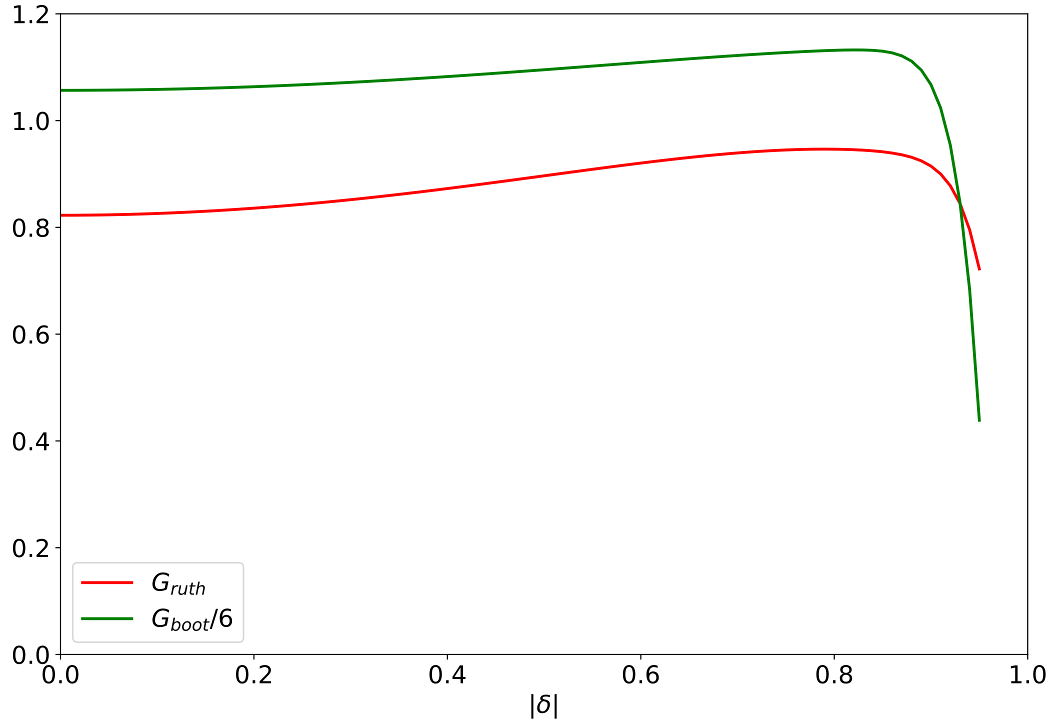

FIG. 8. The integrals $G_{\rm ruth}$ and $G_{\rm boot}/6$ evaluated as functions of the modulus of the island asymmetry parameter, $|\delta|$.

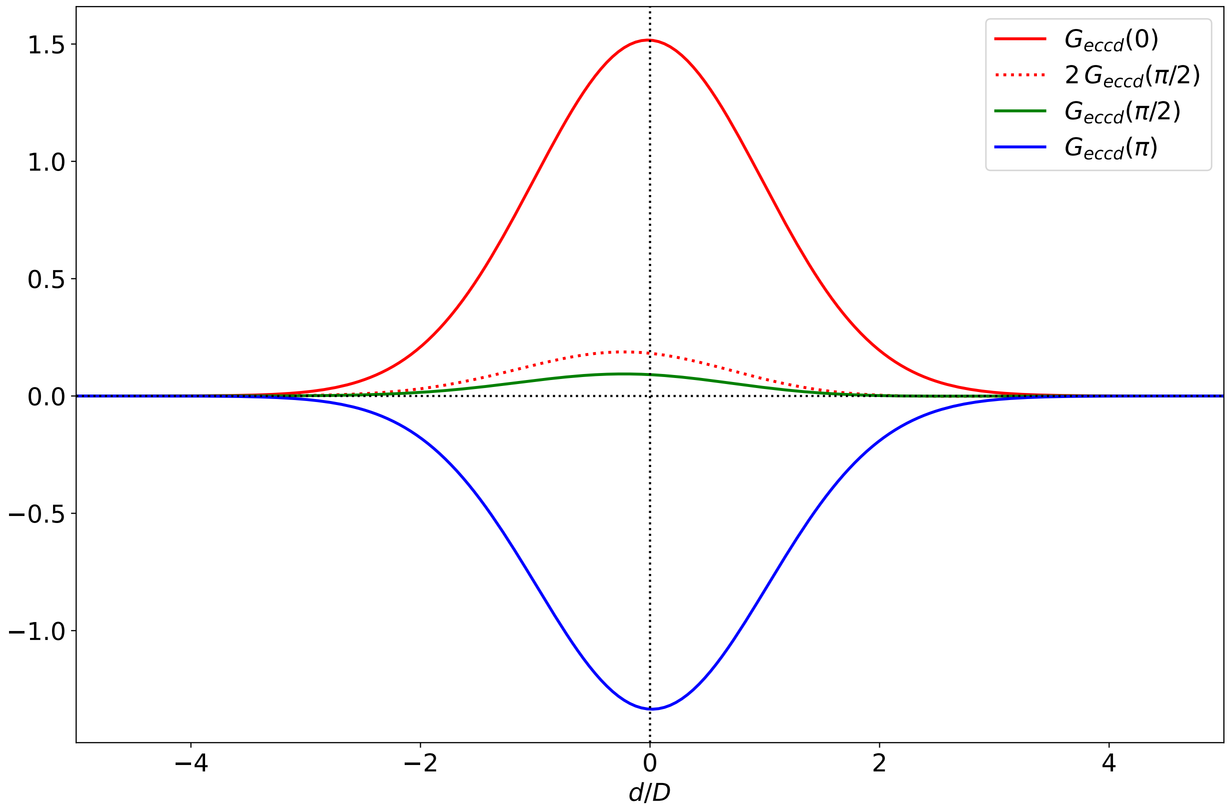

FIG. 9. The integral $G_{\rm eccd}(\Delta\zeta)$ evaluated as a function of d/D at $\Delta\zeta = 0$, $\pi/2$, and π for an island of full width $W = 0.1\,D$ and asymmetry parameter $\delta = 0.5$. The dotted curve shows the integral when the driven current profile is independent of ζ.

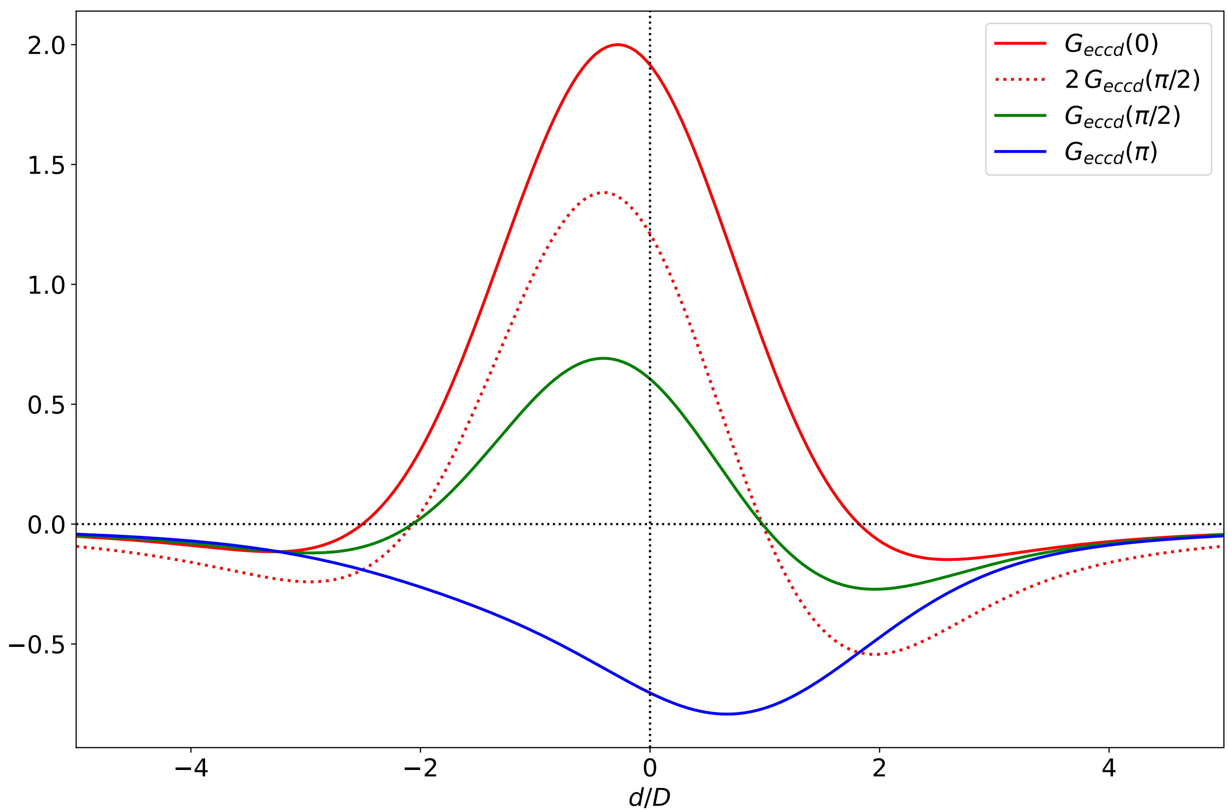

FIG. 10. The integral $G_{\rm eccd}(\varDelta\zeta)$ evaluated as a function of d/D af $\varDelta\zeta = 0$, $\pi/2$, and π for an island of full width $W = 2.0\,D$ and asymmetry parameter $\delta = 0.5$. The dotted curve shows the integral when the driven current profile is independent of ζ.

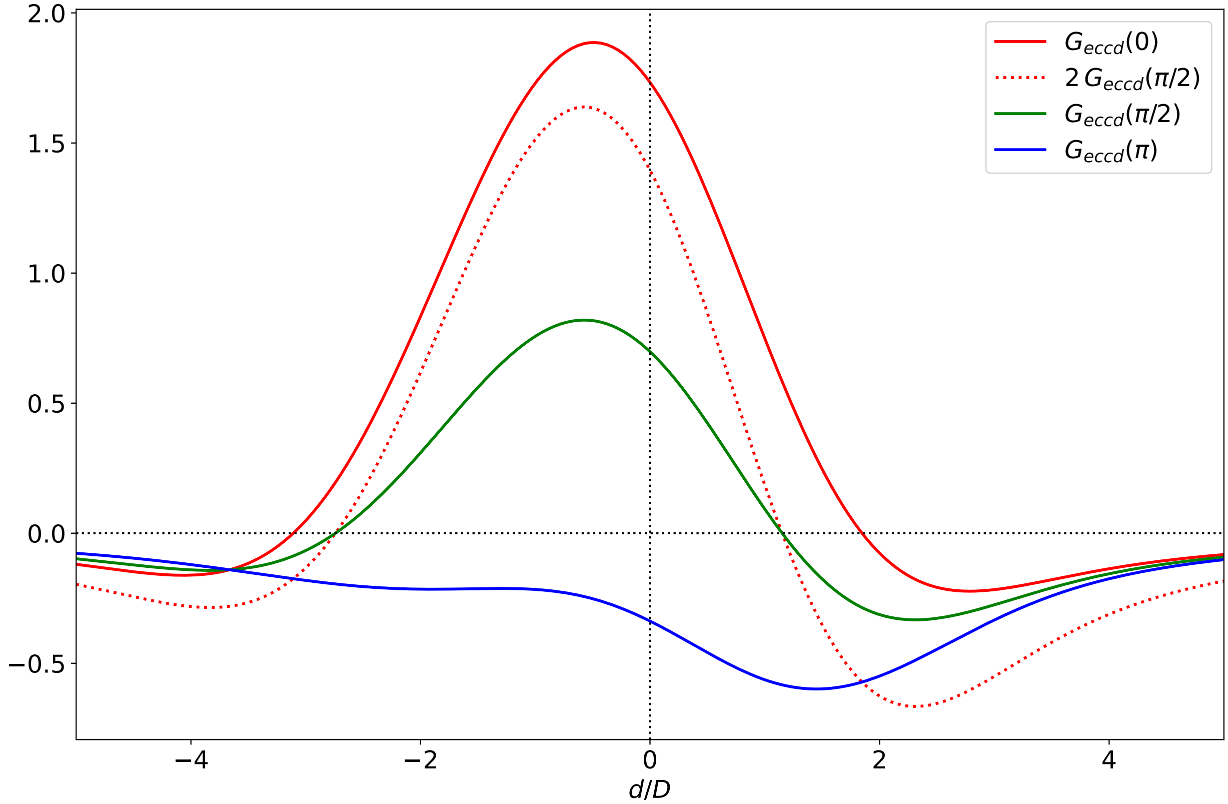

FIG. 11. The integral $G_{\rm eccd}(\varDelta\zeta)$ evaluated as a function of d/D at $\varDelta\zeta = 0$, $\pi/2$, and π for an island of full width $W = 4.0\,D$ and asymmetry parameter $\delta = 0.5$. The dotted curve shows the integral when the driven current profile is independent of ζ.

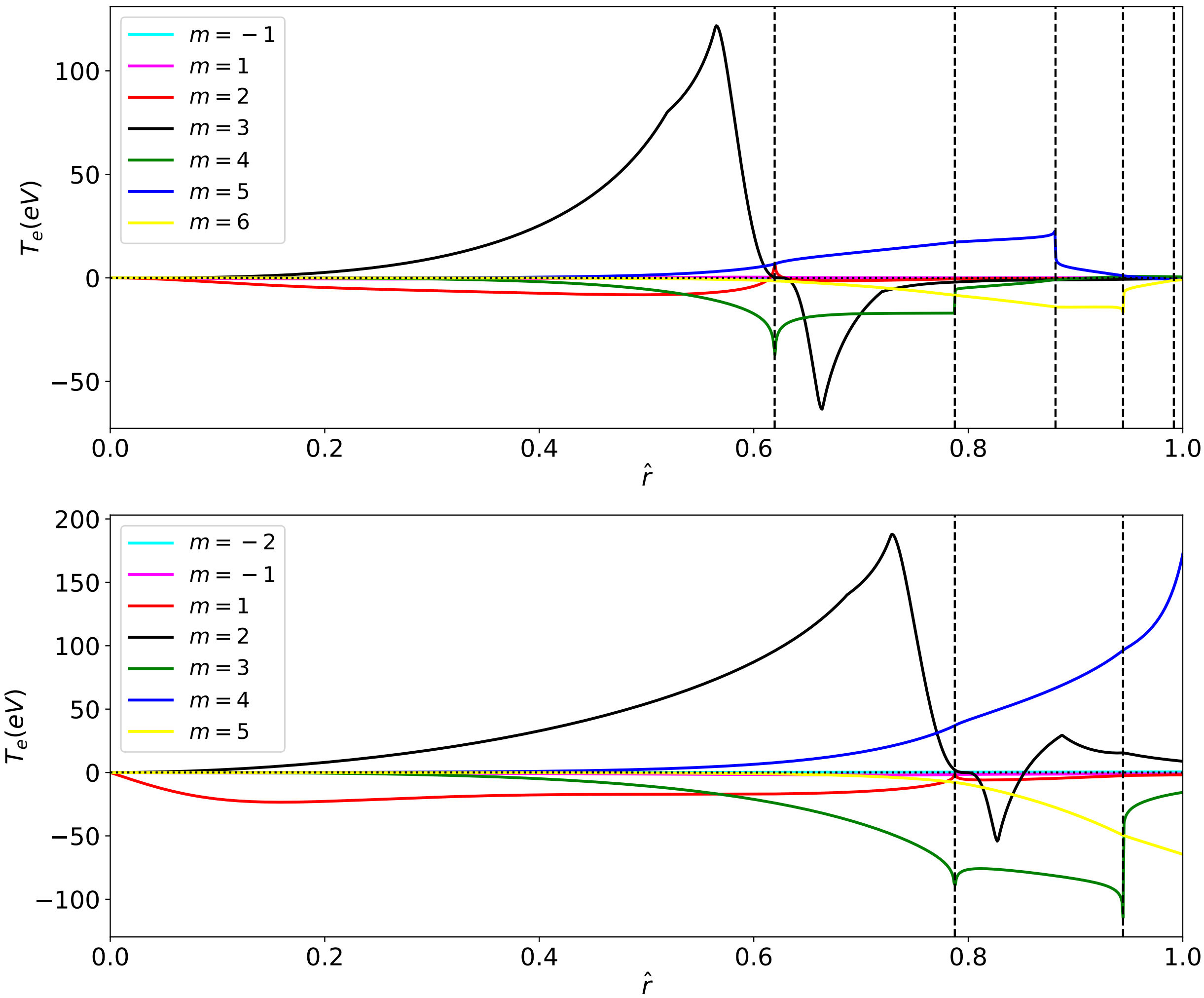

FIG. 12. Harmonics of the perturbed electron temperature associated with a 3, 2 (top panel) and a 2, 1 (bottom panel) NTM of island width $W = 0.1\,a$ in the example plasma equilibrium pictured in Figs. 1 and 2. The harmonics all have the same toroidal mode number as the NTM. The vertical dashed lines show the positions of the rational surfaces.

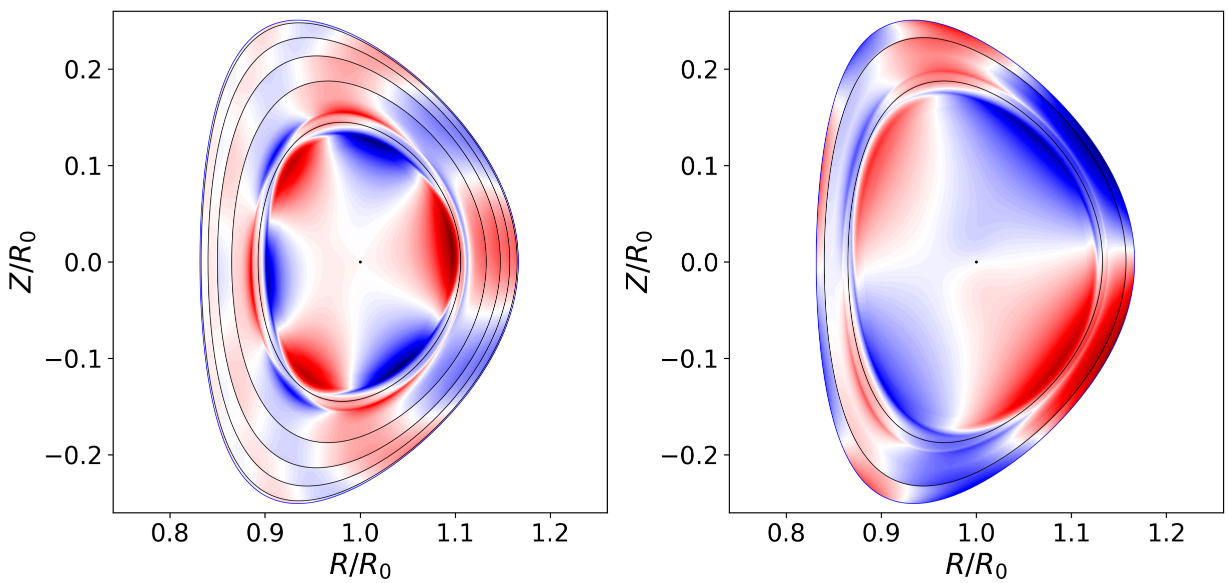

FIG. 13. Electron temperature perturbation at a particular toroidal angle associated with a 3, 2 (left panel) and a 2, 1 (right panel) NTM of island width $W = 0.1\,a$ in the example plasma equilibrium pictured in Figs. 1 and 2. The black curves show the locations of the rational surfaces. The black dot shows the location of the magnetic axis.

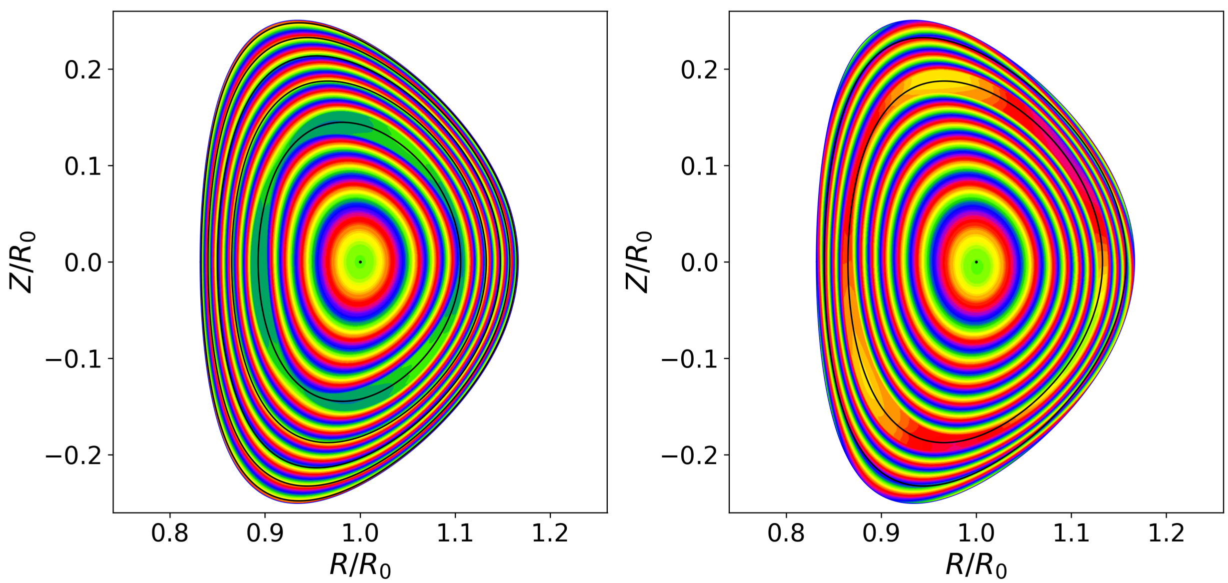

FIG. 14. Total electron temperature at a particular toroidal angle (which is the same as that in Fig. 13) associated with a 3, 2 (left panel) and a 2, 1 (right panel) NTM of island width $W = 0.1\,a$ in the example plasma equilibrium pictured in Figs. 1 and 2. The black curves show the locations of the rational surfaces. The black dot shows the location of the magnetic axis.

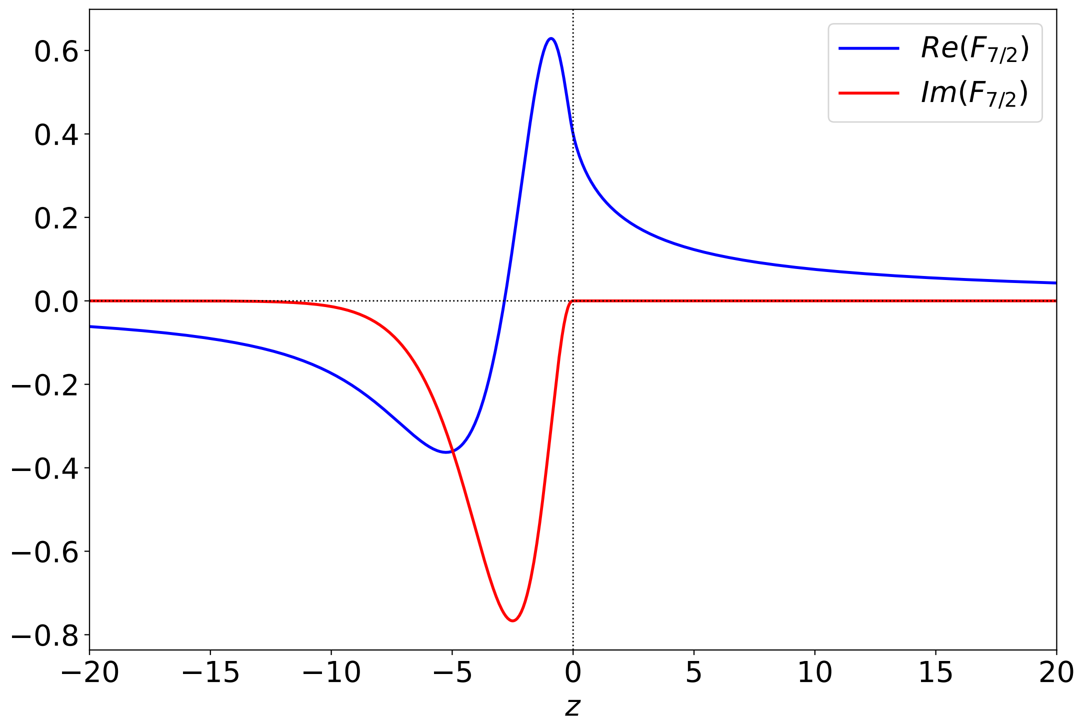

FIG. 15. The real and imaginary parts of the function $F_{7/2}(z)$.

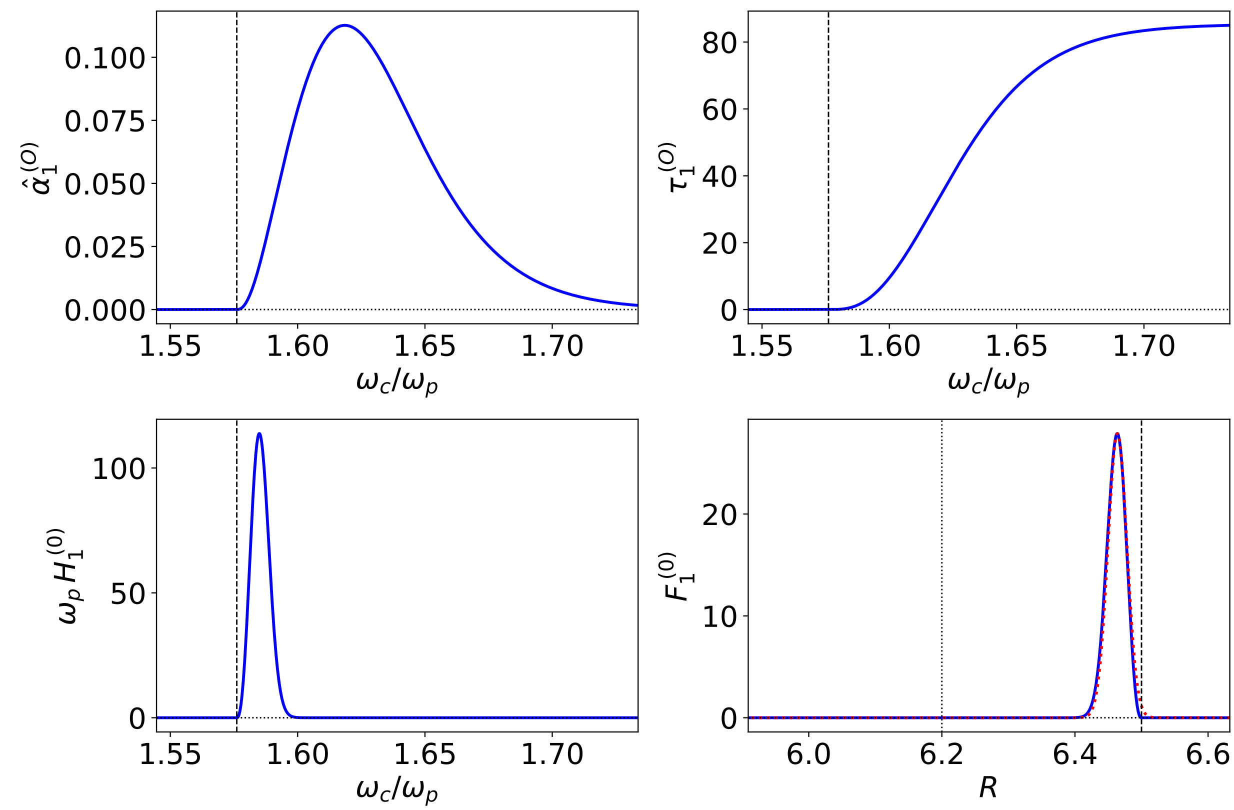

FIG. 16. The normalized absorption coefficient (top left), optical depth (top right), normalized spectral convolution function (bottom left), and spatial convolution function (bottom right), for 1st harmonic O-mode ECE from an ITER-like plasma characterized by $T_e = 5\,\mathrm{keV}$, $n_e = 10^{20}\,\mathrm{m}^{-3}$ (at the cyclotron resonance), $B_0 = 5.3\,\mathrm{T}$, $R_0 = 6.2\,\mathrm{m}$, and $R_\omega = 6.5\,\mathrm{m}$. The vertical dashed lines show the location of the cyclotron resonance. The vertical dotted line (in the bottom right panel) shows the location of the major radius.

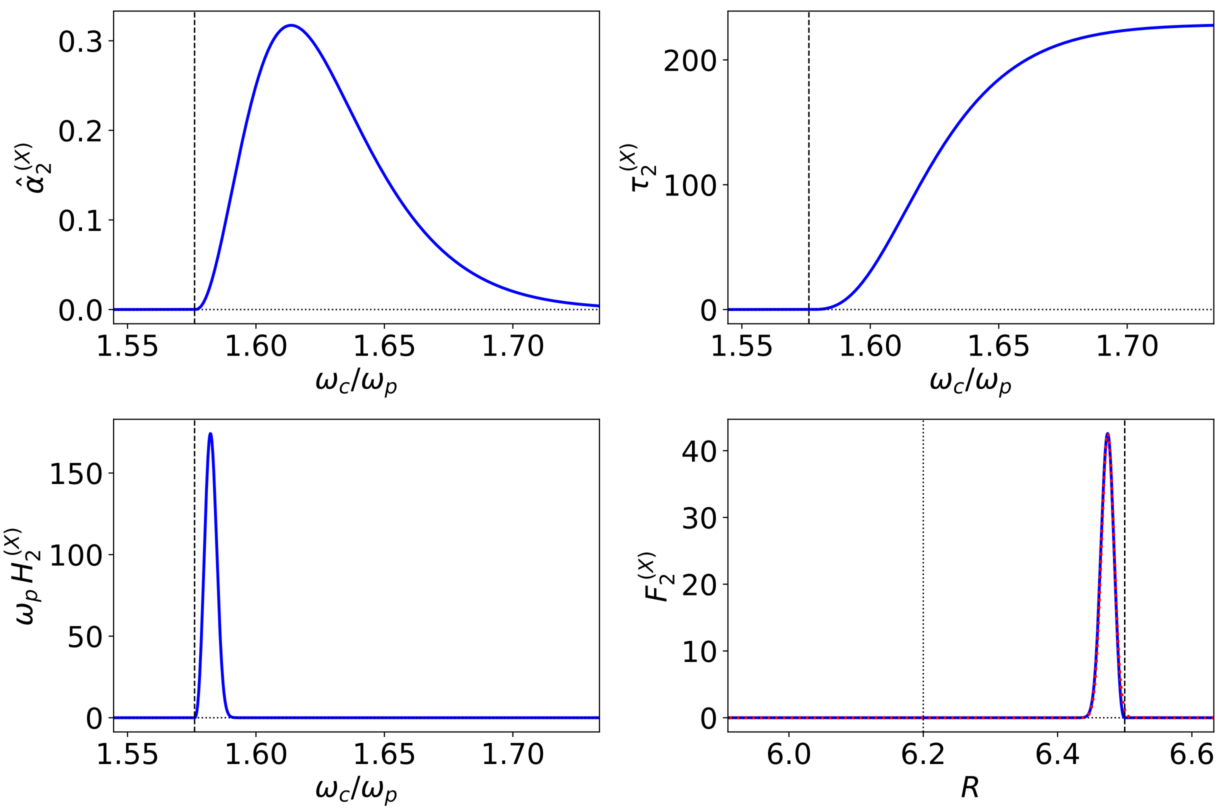

FIG. 17. The normalized absorption coefficient (top left), optical depth (top right), normalized spectral convolution function (bottom left), and spatial convolution function (bottom right), for 2nd harmonic X-mode ECE from the same ITER-like plasma as that considered in the previous figure. See previous figure caption.